Title

Large-scale mass wasting on the Miocene continental margin of western India

Journal
GEOLOGICAL SOCIETY OF AMERICA BULLETIN, 132(1-2)

ISSN
0016-7606

Authors
Dailey, Sarah K
Clift, Peter D
Kulhanek, Denise K
et al.

Publication Date
2020

DOI
10.1130/B35158.1

Peer reviewed

BULLETIN
THE GEOLOGICAL SOCIETY OF AMERICA®

E: gsab@geosociety.org
W: geosociety.org/gsa
T: @geosociety

Large-scale Mass Wasting on the Miocene Continental Margin of Western India

Tracking no: B35158

Authors:
Sarah Dailey (Louisiana State University), Peter Clift (Louisiana State University), Denise Kulhanek, Jerzy Blusztajn (WHOI), Claire Routledge (University College), Gérôme Calvès (Universite Toulouse III Paul Sabatier), Paul O'Sullivan (Geosep Services), Tara Jonell (University of Queensland), Dhananjai K Pandey, Sergio Ando (Universita degli Studi di Milano-Bicocca Dipartimento di Scienze dell'Ambiente e del Territorio e di Scienze della Terra), Giovanni Coletti (Universita degli Studi di Milano-Bicocca Dipartimento di Scienze dell'Ambiente e del Territorio e di Scienze della Terra), Peng Zhou (Louisiana State University), Yuting Li (Purdue University), Nikki Neubeck (Louisiana State University), James Bendle, Sophia Bratenkov (Macquarie University), Elizabeth Griffith (Ohio State University), Gundiga Gurumurthy (Manipal University), Annette Hahn (Bremen University), Masao Iwai (Kochi University), Boo-Keun Khim (Pusan National University), Anil Kumar (Wadia Institute of Himalayan Geology), A. Ganesh Kumar (National Institute of Ocean Technology), Hannah Liddy (Columbia University), Huayu Lu (Nanjing University), Mitchell Lyle (Oregon State University), Ravi Mishra (National Centre for Antarctic and Ocean Research), Tallavajhala Radhakrishna (Centre for Earth Science Studies), Rajeev Saraswat (National Institute of Oceanography), Rakesh Saxena (ONGC), Giancarlo Scardia (Universidade de São Paulo), Girish Sharma (Kumaun University), Arun Singh (Banaras Hindu University), Stephan Steinke (Department of Geological Oceanography), Kenta Suzuki (Hokkaido University), Lisa Tauxe, Manish Tiwari (National Centre for Antarctic and Ocean Research), Zhaokai Xu (Institute of Oceanology, Chinese Academy of Sciences), and Zhaojie Yu (University of Paris XI)

Abstract:
A giant mass transport complex was recently discovered in the eastern Arabian Sea, exceeding in volume all but one other known complex on passive margins worldwide. The complex, named the Nataraja Slide, was drilled by International Ocean Discovery Program (IODP) Expedition 355 in two locations where it is ~300 m (Site U1456) and ~200 m thick (Site U1457). The top of this mass transport complex is defined by the presence of both reworked microfossil assemblages and deformation structures, such as folding and faulting. The deposit consists of two main phases of mass wasting, each which consists of smaller pulses, with generally fining-upward cycles, all emplaced just prior to 10.8 Ma. The base of the deposit at each site is composed largely of matrix-supported carbonate breccia that is interpreted as the product of debris flows. In the first phase, these breccias alternate with well-sorted calcarenites deposited from a high energy current, coherent limestone blocks that are derived directly from the Indian continental margin, and a few clastic mudstone beds. In the second phase, at the top of the deposit, muddy turbidites dominate and become increasingly more siliciclastic. At Site U1456, where both phases are seen, a 20 m section of hemipelagic mudstone is present, overlain by a ~40 m thick section of calcarenite and slumped interbedded mud and siltstone. Bulk sediment geochemistry, heavy- mineral analysis, clay mineralogy, isotope geochemistry, and detrital zircon U-Pb ages constrain the provenance of the clastic, muddy material to being reworked Indus-derived sediment, with input from western Indian rivers (e.g., Narmada and Tapti Rivers), and some material from the Deccan Traps. The carbonate blocks found within the breccias are shallow-water limestones from the outer western Indian continental shelf that was oversteepened from enhanced clastic sediment delivery during the mid-Miocene. The final emplacement of the material was likely related to seismicity as there are modern analogues for intraplate earthquakes close to the source of the slide. Although we hypothesize this area is at low risk for future mass wasting events, it should be noted that other oversteepened continental margins around the world could be at risk for mass failure as large as the Nataraja Slide.

Large-scale Mass Wasting on the Miocene Continental Margin of Western India

Sarah K. Dailey[1], Peter D. Clift[1], Denise K. Kulhanek[2], Jerzy Blusztajn[3], Claire M. Routledge[4], Gérôme Calvès[5], Paul O'Sullivan[6], Tara N. Jonell[7], Dhananjai K. Pandey[8], Sergio Andò[9], Giovanni Coletti[9], Peng Zhou[1], Yuting Li[1], Nikki E. Neubeck[1], James A.P. Bendle[10], Sophia Bratenkov[11], Elizabeth M. Griffith[12], Gundiga P. Gurumurthy[13], Annette Hahn[14], Masao Iwai[15], Boo-Keun Khim[16], Anil Kumar[17], A. Ganesh Kumar[18], Hannah M. Liddy[19], Huayu Lu[20], Mitchell W. Lyle[21], Ravi Mishra[8], Tallavajhala Radhakrishna[22], Rajeev Saraswat[23], Rakesh Saxena[24], Giancarlo Scardia[25], Girish K. Sharma[26], Arun D. Singh[27], Stephan Steinke[28], Kenta Suzuki[29], Lisa Tauxe[30], Manish Tiwari[9], Zhaokai Xu[31], and Zhaojie Yu[32]

1 - Department of Geology and Geophysics, Louisiana State University, E253 Howe-Russell-Kniffen Geoscience Complex, Baton Rouge LA 70803, USA

2 - International Ocean Discovery Program, Texas A&M University, 1000 Discovery Drive, College Station, TX 77845, USA

3 – Department of Geology and Geophysics, Woods Hole Oceanographic Institution, Woods Hole, MA 02543, USA

4 - Department of Earth Sciences, University College London, Gower Street, London, WC1E 6BT, United Kingdom

5 - Université Toulouse 3, Paul Sabatier, Géosciences Environnement Toulouse, 14 avenue Edouard Belin, 31400, Toulouse, France

6 - GeoSep Services, 1521 Pine Cone Road, Moscow, Idaho 83843 USA

7 - School of Earth and Environmental Sciences, University of Queensland, QLD 4072, Australia

8 - National Centre for Antarctic and Ocean Research (NCAOR), Vasco da Gama, Goa 403804, India

9 - Department of Earth and Environmental Sciences, University of Milano Bicocca, Piazza della Scienza 4, 20126 Milan, Italy

10 - School of Geography, Earth and Environmental Sciences, University of Birmingham, Edgbaston, Birmingham B15 2TT, United Kingdom

11 - Department of Earth and Planetary Sciences, Macquarie University, 202/1 Botany Rd., Sydney NSW 2017, Australia

12 - School of Earth Sciences, Ohio State University, 275 Mendenhall Lab, 25 South Oval Mall, Columbus OH, 43210, USA

13 - Manipal Centre for Natural Sciences, Manipal University, Manipal 576104, India

14 – MARUM, University of Bremen, Leobener Strasse, Bremen 28359, Germany

15 - Department of Natural Environmental Science, Kochi University, 2-5-1 Akebono-cho, Kochi 780-8520, Japan

16 - Division of Earth Environmental System, Pusan National University, Jangjeon-dong, Geumjeong-gu, Busan 609-73, Korea

17 - Department of Science and Technology Wadia Institute of Himalayan Geology, 33 GMS Road, Dehradun, Uttrakhand 248001, India

18 - Marine Biotechnology Department, National Institute of Ocean Technology, Velachery-Tambaram Main Road, Pallikaranai, Chennai 600100, India

19 - The Earth Institute, Columbia University, Hogan Hall, 2910 Broadway, Level A, New York NY 10025, USA

20 - School of Geographical and Oceanographical Sciences, Nanjing University, 163 Xianlin Avenue, Nanjing 210023, P.R. China

21 - College of Earth, Ocean and Atmospheric Sciences, Oregon State University, 104 CEOAS Administration Building, Corvallis OR 97331, USA

22 - Geosciences Division, National Centre for Earth Science Studies, Aakkulam Trivandrum 695031, India

23 - Geological Oceanography Division, National Institute of Oceanography, Dona Paula, Goa 403004, India

24 – ONGC, 11 High, Bandra-Sion Link Road, Mumbai 400017, India

25 - Instituto de Geociências e Ciências Exatas, Universidade Estadual Paulista, 1515 Avenida 24-A, Rio Claro SP 13506-900, Brazil

26 - Department of Geology, Kumaun University, Nainital 263002, India

27 - Department of Geology, Banaras Hindu University, Varanasi Uttar Pradesh 221005, India

28 - Department of Geological Oceanography and State Key Laboratory of Marine Environmental Science, Xiamen University, Xiamen 361102, P.R. China

29 - Graduate School of Environmental Science, Hokkaido University, N10W5, Kita-ku, Sapporo 060-0810, Japan

30 - Scripps Institution of Oceanography, 9500 Gilman Drive, La Jolla CA 92093-0220, USA

31 - Key Laboratory of Marine Geology and Environment, Institute of Oceanology, Chinese Academy of Sciences, 7 Nanhai Road, Qingdao Shandong 266071, P.R. China

32 - University of Paris XI (Orsay), Bâtiment 504, Orsay Cedex 91405, France

Abstract

A giant mass-transport complex was recently discovered in the eastern Arabian Sea, exceeding in volume all but one other known complex on passive margins worldwide. The complex, named the Nataraja Slide, was drilled by International Ocean Discovery Program (IODP) Expedition 355 in two locations where it is ~300 m (Site U1456) and ~200 m thick (Site U1457). The top of this mass transport complex is defined by the presence of both reworked microfossil assemblages and deformation structures, such as folding and faulting. The deposit consists of two main phases of mass wasting, each which consists of smaller pulses, with generally fining-upward cycles, all emplaced just prior to 10.8 Ma. The base of the deposit at each site is composed largely of matrix-supported carbonate breccia that is interpreted as the product of debris flows. In the first phase, these breccias alternate with well-sorted calcarenites deposited from a high energy current, coherent limestone blocks that are derived directly from the Indian continental margin, and a few clastic mudstone beds. In the second phase, at the top of the deposit, muddy turbidites dominate and become increasingly more siliciclastic. At Site U1456, where both phases are seen, a 20-m section of hemipelagic mudstone is present, overlain by a ~40 m thick section of calcarenite and slumped interbedded mud and siltstone. Bulk sediment geochemistry, heavy-mineral analysis, clay mineralogy, isotope geochemistry, and detrital zircon U-Pb ages constrain the provenance of the clastic, muddy material to being reworked Indus-derived sediment, with input from western Indian rivers (e.g., Narmada and Tapti Rivers), and some material from the Deccan Traps. The carbonate blocks found within the breccias are shallow-water limestones from the outer western Indian continental shelf that was oversteepened from enhanced clastic sediment delivery during the mid-Miocene. The final emplacement of the material was likely related to seismicity as there are modern analogues for

intraplate earthquakes close to the source of the slide. Although we hypothesize this area is at low risk for future mass wasting events, it should be noted that other oversteepened continental margins around the world could be at risk for mass failure as large as the Nataraja Slide.

INTRODUCTION

Large-scale mass wasting of continental margins is an important process in controlling the geomorphology of continental slopes fringing all ocean basins (Coleman and Prior, 1988). The scale of large mass transport complexes (MTCs) makes them significant as geohazards, directly through mass wasting (Dan et al., 2007; Yamada et al., 2012), by generating tsunami~~s~~ (Tappin et al., 2001), as well as posing risks for seafloor infrastructure such as oil and gas platforms, pipelines (Bea et al., 1983), and communication cables (Hsu et al., 2008). Moreover, the emplacement of ~~MTCs~~ can have significant influence on the stratigraphy of deep ocean basins, as well as for the continental margin from which it was derived.

Although the largest mass transport deposits are associated with active margins (Burg et al., 2008), where earthquakes are more common and can act as triggers for emplacement, passive margins are also recognized to host some of the largest gravitational collapses in the modern oceans (Embley and Jacobi, 1977). Seismic surveying in the eastern Arabian Sea offshore western India has identified one of the largest such complexes, totaling around 19,000 km^3 (Calvès et al., 2015). Mapping of the deposit by seismic methods suggests that it may be up to 800 m thick in places (Calvès et al., 2015). In 2015 this deposit was drilled by International Ocean Discovery Program (IODP) during Expedition 355. During the expedition, the MTC was sampled on its southern edge, where the thicknesses were considerably thinner (Pandey et al., 2016c)(Fig. 1). The deposit, named the Nataraja Slide, shows substantial run out from its inferred source regions offshore Saurashtra (Fig. 1), being emplaced ~500 km into the Indian Ocean. In this study, we examine the sedimentary rocks recovered by IODP in order to infer the depositional mechanisms active during emplacement. We further make inferences about what processes triggered its formation, which is dated as being just before 10.8 Ma (Pandey et al., 2016a). Are MTCs of this magnitude formed by the same processes that we see at much smaller scales, or are these mega-scale complexes unique in their modes of emplacement and triggers? Given the profound potential geohazards for human settlements in coastal regions, understanding the origins and impacts of the Nataraja Slide ~~MTC~~ are of both great scientific and societal significance.

GEOLOGY OF LARGE ~~MTCS~~

Mass transport complexes are an extreme form of gravity induced sediment transport (Hampton et al., 1996). Most submarine gravity driven sediment transport involves redeposition of individual sediment particles suspended in water (e.g., in a turbidity current) or as a fluidized sediment suspension (e.g., a debris flow or mud flow)(Pickering et al., 1986; Talling et al., 2012). Sediment may also be mobilized when the proportion of water is very low, such as a slow-moving sediment grain flow or creep (Carter, 1975; Lowe, 1976). However, large volumes of material can also be transported rapidly (hours to days) in the form of slope failures where coherent masses of material can be transported by sliding, rolling, falling, and/or slumping (Coleman and Prior, 1988). Slumps involve displacement of a stratigraphic package above a concave-upward detachment surface and can leave the slumped material in a relatively undisturbed state after removal from an area that then shows an arcuate scar (Hampton et al., 1996; Moore, 1961). Slumps differ from slides in that motion is along a pre-existing weakness, such as a bedding plane or joint surface, but the displaced package can move as a coherent mass, or can be become disaggregated depending on the length and speed of transport. Significant progress has been made in understanding mass transport through outcrop studies, such as the Carboniferous (Pennsylvanian) Ross Slide of Ireland (Martinsen and Bakken, 1990; Strachan, 2002), the Eocene of the Pyrenean foreland basin (Farrell, 1984), and the Pliocene of Sicily (Trincardi and Argnani, 1990). In all examples, each MTC was emplaced over a sharply defined basal décollement once the deposit reached the lower slope after erosive mass wasting of the steeper upper slope.

The geometry and internal structure of any gravitationally driven slump, slide or debris flow reflect the mechanism of failure and the morphology of the slope where the transport occurs (Lucente and Pini, 2003). The style of deformation and the mode of transport are controlled by sediment and rock rheology that in turn are dependent on the lithology and strain rate. For this reason, the largest MTCs are different from shallow debris flows and slumps because they incorporate both lithified and unconsolidated materials. There are few exposures of very large MTCs and those in the oceans are hard to access, especially through drilling. MTCs are often seismically homogeneous (Vardy et al., 2010) but can show important changes in sediment facies with depth and with distance from their source. For example, swath bathymetric mapping of the Ebro margin in the western Mediterranean featuring the pre-11 ka BIG'95 Slide shows that only finer sediments have reached the most distal areas, yet coherent rafts of continental margin sedimentary rock are seen at the base of the slope (Lastras et al., 2004). Analysis of the geometry and distribution of sedimentary facies and structures can be used to reconstruct the evolving sedimentary and deformational strain history of any individual MTC. By doing so, it is possible to derive a kinematic model of emplacement that can be compared with other examples.

The Storegga Slide in offshore Norway is one of the best studied large-volume mass transport complex. This MTC is entirely siliciclastic and its generation has been linked to sliding on contourite sand and silts that became overpressured as a result of rapid burial by glacial maximum aged debris-flow sediments (Bryn et al., 2005). However, rapid sedimentation on any clastic margin receiving sediment from the continent would provide weak layers on which sliding could occur. Overpressuring has also been linked to growth and migration of silica diagenetic fronts (Davies and Clark, 2006). Slope oversteepening increases the chances of mass wasting simply by the consequence of rapid sediment delivery, although the tendency may be heightened by the pre-existing basement structure of the continental margin (Lastras et al., 2004). Slope oversteepening by itself cannot explain large-scale mass wasting because giant MTCs on European continental margins are mostly associated with low gradient glacial margins. In contrast, turbidity currents appear to dominate on steeper non-glacial margins ~~which~~ might otherwise be expected to suffer mass wasting due to their gradient (Leynaud et al., 2009). In these cases, differences in the sediment types and the timing of sediment delivery favor gravitational instabilities at different times, with non-glaciated margins tending to mass waste more during sealevel lowstands, where the opposite more often occurs on glaciated margins. Modelling indicates that continental margins with more cohesive clay-rich sediments tend to experience coherent sliding more frequently than sand-rich margins whose gravitational slides tend to disintegrate into turbidity currents (Elverhoi et al., 2010).

The triggering of ~~MTC emplacement~~ can be attributed to a number of potential processes, including seismicity (Moernaut et al., 2007; Piper et al., 1985), volcanic eruptions (Carracedo, 1999) and meteorite impacts (Klaus et al., 2000; Parnell, 2008). Dissociation of gas hydrates during times of warming seawater could have aided liquefaction in the case of Storegga Slide

(Mienert et al., 2005), with seismicity possibly related to post-glacial isostatic rebound providing the final impetus for redeposition (Evans et al., 2002). In the eastern Mediterranean Sea, MTC emplacement has also be linked to biogenic gas and slope oversteepening acting individually or in tandem with one another (Frey Martinez et al., 2005).

Mechanisms for MTC emplacement differ between clastic and carbonate margins. This is because carbonate sediment production occurs *in situ* and can result in steep platform margins, sometimes almost vertically where reef complexes develop in outer shelf areas. Carbonate production is strongly linked to sealevel and was fastest when sealevel was high after the onset of Northern Hemispheric Glaciation (NHG, ~2.4 Ma)(Schlager et al., 1994). Many carbonate MTCs are linked to platform margin collapse and result in deposits with numerous coherent blocks suspended within a more fluidized matrix. Seismic mapping around the Great Bahama Bank has identified coherent Plio-Pleistocene sedimentary rock rafts 0.5–2.0 km in length, 0.3–1.5 km in width, and 50 m in thickness (Principaud et al., 2015). Adjacent deposits have also been observed on the Florida margin (Mullins et al., 1986), as well as offshore Nicaragua (Hine, 1992), all with a similar Plio-Pleistocene age. Plio-Pleistocene MTCs are larger than most known older examples because the rapidly changing sealevel since the start of the ~~NHG~~ enhanced carbonate production and induced gravitational instability as sealevel rose and fell (Schlager et al., 1994). Among these older deposits, only the Cretaceous Ayabacas MTC of Peru is noteworthy for its large volume, long run out and presence of slide blocks measuring kilometers in length (Callot et al., 2008).

GEOLOGICAL SETTING

The Nataraja Slide lies within the Laxmi Basin offshore the western continental margin of India (Fig. 1A and B). The Laxmi Basin is separated from the main Arabian Basin by the Laxmi Ridge (Fig. 1). The Laxmi Basin is a rift basin that formed between India and the Laxmi Ridge prior to the opening of the main Arabian Sea ~~in the early Paleocene~~ (Bhattacharya et al., 1994), where the ridge is generally interpreted to be a rifted fragment of Indian continental crust (Pandey et al., 1995). The age of rifting is somewhat controversial, but likely just predates the emplacement of the Deccan Traps flood basalts in the latest Cretaceous, based on analysis of magnetic anomalies (Bhattacharya et al., 1994) and the geochemistry of the basalts sampled at IODP Site U1457 (Pandey et al., 2016b). The sediments in the Laxmi Basin can be divided into three major units described below. The oldest, dated as Lower Paleocene, largely comprises red-brown mudstones eroded from peninsular India and sampled at IODP Site U1457 (Pandey et al., 2016b). These deposits are overlain by the Nataraja Slide and by younger distal turbidite sandstones and siltstones, as well as hemipelagic mudstones that form the Indus submarine fan. These latter sediments were supplied through the Indus River via erosion from the western Himalaya and Karakoram (Pandey et al., 2016c). The age of the Indus Fan in the Laxmi Basin is not well defined, although within the main Arabian basin the fan is typically considered to date from at least 45 Ma, continuing to the present time (Clift et al., 2001). It is within these deposits that the Nataraja Slide (MTC) was emplaced just before 10.8 Ma.

Towards the east, the Laxmi Basin is bounded by the rifted passive margin of India, which has been supplied by sediment from the erosion of the peninsula via a number of significant rivers that drain towards the west (e.g., Mahi, Tapti, and Narmada). Oil exploration drilling has furthermore identified significant repeated buildups of carbonate on the shelf, especially towards the shelf edge where the supply of clastic material was more limited (Rao and

Talukdar, 1980; Wandrey, 2004). It is generally presumed that extensional deformation in the area ceased after the rifting that formed the Laxmi Basin. The area has been largely seismically inactive except towards the north where the Rann of Kutch forms an active structure within the Indian Craton. This structure is linked to flexure of the plate as a result of the collision between India and Asia (Bilham et al., 2003; Biswas, 2005), presumed to have started in the Eocene (Najman et al., 2010) or even earlier (DeCelles et al., 2014). Towards the north, the Indian peninsula is cut by the NE-SW-trending Cambay Basin which formed as an initial early Cretaceous rift that was then reactivated in the Cenozoic and experienced significant inversion in the early Miocene (Chowdhary, 2004).

The MTC run-out distance is estimated to be about 550 km, with a length of 338 km and a maximum width of 193 km (Calvès et al., 2015). Prior work on the Nataraja Slide found this MTC to be acoustically homogenous in seismic lines, with few identified rafts present and to have a flat, rather than significantly angular erosive base over older deposits (Fig. 2)(Calvès et al., 2015; Pandey et al., 2016c). However, closer inspection in the vicinity of the drilling sites finds this is not always the case. In the case of IODP Site U1456 where the slide is somewhat thicker, there is a significant missing section of submarine fan turbidites from ~15.6 to 10.8 Ma (Pandey et al., 2016a). In that area the upper part of the deposit appears to be more acoustically washed out and homogenous, but the lower regions are marked by strong reflections that show limited lateral continuity suggestive of some internal structure within the deposit. This raises the possibility that this is not simply a single depositional package (Fig. 2). Such strong reflections are reminiscent of coherent slide blocks seen in seismic images of other MTCs (Gamboa et al., 2012; Krastel et al., 2012; Principaud et al., 2015). The same is not true at the more distal Site

U1457 location where the MTC onlaps the Laxmi Ridge and its acoustic character is more uniform.

METHODS

Sedimentary cores were collected and initially described during IODP Expedition 355, but several cores are re-examined in order to obtain more detailed descriptions of critical sedimentary structures and facies. In addition to preparing sedimentary logs designed to highlight the contrasting sedimentary facies, samples for sediment petrography were examined to allow investigation into the different sediment types at both the macro and microscopic scale. These methods allowed us to better define the depositional processes that operated during Nataraja Slide emplacement and to provide constraints on the origin(s) of the MTC.

Geochemical methods were employed in order to further constrain the provenance of the materials, and in particular, to verify the proposed western Indian continental margin source for much of the MTC argued by Calvès et al. (2015). This approach is predicated on the fact that source rocks of MTC deposits have different bulk geochemical compositions and that Himalayan sources can be effectively discriminated from peninsular sources when considering provenance due to different bedrock source compositions and contrasting chemical weathering histories.

Forty-four samples were selected for determination of major element composition, together with select trace elements (Ni, Ba, V, Zr, Sc, Y, Sr). These were determined by inductively coupled plasma emission spectrometry (ICP-ES) at Boston University, with precision quantified to be better than 2% of the measured value for all elements. Accuracy was constrained by analysis of certified Standard Reference Materials (BHVO-2) and results were accurate within precision. Table 1 provides analyses of samples as well as repeated analyses of the standard.

The neodymium (Nd) isotope compositions of sediments are generally considered to be minimally affected by chemical weathering, such that source terranes faithfully translate their isotopic signature to eroded sediments (i.e., Goldstein et al. ((1984))) and can be utilized for sedimentary provenance studies. Strontium (Sr) isotopes are additionally considered, while recognizing that Sr isotope compositions may be affected by chemical alteration largely during transport across flood plains (Derry and France-Lanord, 1996). Together these isotopic systems have a record of being powerful provenance proxies in the Arabian Sea (e.g., ((Clift and Blusztajn, 2005; Clift et al., 2008a))). Care was taken to decarbonate samples prior to analysis with 20% acetic acid because Sr isotope compositions are strongly controlled by carbonate compositions and this study targets the siliciclastic sediment compositions only. Decarbonation lasted for six days until no further fizzing was observed when samples were exposed to unreacted acid. Samples were washed by deionized water before being ground into powders. Twenty-five samples were selected throughout the Nataraja Slide/MTC at Sites U1456 and U1457 for the determination of $^{143}Nd/^{144}Nd$ and $^{87}Sr/^{86}Sr$ values. Isotopic compositions were determined by Finnigan Neptune multi-collector inductively coupled plasma mass spectrometer (MC-ICP-MS) at the Woods Hole Oceanographic Institute for both Nd and Sr isotopes. Nd and Sr isotope analyses were corrected against La Jolla Nd standard $^{143}Nd/^{144}Nd=0.511847$ and NBS987 standard $^{87}Sr/^{86}Sr=0.710240$. Procedural blanks were 20–25 pg for Sr and 50–70 pg for Nd. We calculate the parameter ϵ_{Nd} after (DePaolo and Wasserburg, 1976) using a $^{143}Nd/^{144}Nd$ value of 0.512638 for the Chondritic Uniform Reservoir (CHUR) (Hamilton et al., 1983). Results are presented in Table 2.

Heavy-mineral analysis was applied to study the mineralogy of the MTC deposits in order to further constrain the source of the materials and to estimate the potential impact of diagenetic dissolution. Sediment left after thin section preparation was gently crushed in water with mortar and pestle and wet-sieved using a standard 500 μm steel sieve and a special handmade 15 μm tissue-net sieve. A wide size window (15–500 μm) was chosen to include a large range of the size distribution (Garzanti et al., 2009). A gravimetric separation of dense grains was achieved with a centrifuge using Na-polytungstate (density 2.90 g/cm^3), and heavy minerals recovered by partial freezing in liquid nitrogen. An appropriate amount of the dense fraction thus obtained was split with a micro-riffle box and mounted with Canada balsam. Heavy minerals were counted under a polarizing microscope with the area method (Mange and Maurer, 1992). Grains of uncertain character were systematically checked and identified by an inViaTM Renishaw Raman spectrometer, equipped with a 532 nm laser and a 50x LWD objective (Andò and Garzanti, 2014). Heavy-mineral and transparent-heavy-mineral concentrations (HMC and tHMC indices of Garzanti and Andò (2007), representing fundamental parameters for unravelling provenance and detecting hydraulic-sorting effects and diagenesis, allow us to distinguish poor (tHMC < 1), and very rich (tHMC > 10) transparent-heavy-mineral suites. The resulting assemblages were compared with those of modern sediments of the Tapti River (sampled at 21°08'40.7" N, 72°44'08.1"E) and Indus River. Results are presented in Table 3.

U-Pb dating of detrital zircon has been widely used for provenance analysis in siliciclastic systems because zircon is a common mineral in continental rocks of many compositions and is chemically and mechanically resistant to weathering during transport (Carter and Bristow, 2003). ~~Furthermore, zircon has a closure temperature of ~750°C for the U/Pb isotope system (Hodges, 2003), making it very robust and unsusceptible to change during multiple stages of recycling.~~ Mineral separation and grain mounting were performed at GeoSep Services (GSS) Laboratory, Moscow, ID. Only one sample was analyzed for zircon U-Pb dating because much of the core lacked suitable layers for this method. Zircons were separated via hand picking and used for age dating as described by Donelick et al. (2005). This process enhances the recovery of all possible grain sizes while minimizing the potential loss of smaller grains within a sample by the use of water-table devices. The method used by Donelick et al. (2005) further ensures the preservation of complete grains by minimizing grain breakage and/or fracturing that can be associated with traditional procedures of isolating individual grains from whole rock samples. Recovered zircon were mostly medium silt to fine sand-sized grains. Epoxy wafers containing zircon grains for laser ablation inductively coupled plasma mass spectrometry (LA-ICP-MS) were polished manually using 3.0 μm and 0.3 μm Al_2O_3 slurries to expose internal zircon grain surfaces. The polished grain surfaces were washed in 5.5 M HNO_3 for 20 sec. at 21°C in order to clean the surfaces prior to introduction into the laser system sample cell.

A total of 51 individual zircon grains were targeted for data collection using a New Wave YP213 213 nm solid state laser ablation system with a 20 μm diameter laser spot size, 5 Hz laser firing rate, and ultra-high purity He as the carrier gas. Isotopic analyses of the ablated zircons were performed using a ThermoScientific Element 2 magnetic sector mass spectrometer using high purity Ar as the plasma gas. Ages from the ratios $^{207}Pb/^{235}U$, $^{206}Pb/^{238}U$, and $^{207}Pb/^{206}Pb$ were calculated for each data scan and checked for concordance. Concordance was defined as overlap of all three ages at the 1σ level. If the number of concordant data scans for a spot was greater than zero, the more precise age from the concordant-scan-weighted ratio $^{207}Pb/^{235}U$, $^{206}Pb/^{238}U$, or $^{207}Pb/^{206}Pb$ was chosen as the preferred age, and whichever exhibited the lower relative error. If zero concordant data scans were observed, the common Pb-corrected age based on isotopic sums of all acceptable scans was chosen as the preferred age. Results of zircon U-Pb dating are shown in Table 4.

Clay mineralogy was examined for provenance purposes based on the concept that different environmental conditions and source terranes can produce characteristic assemblages. This allows us to separate material derived from the Indus River from material more closely linked to peninsular India. Although there may have been some change in mineralogy during initial diagenesis, the relatively shallow burial depths of these cores means that there is no significant thermal diagenesis and we can consider the observed mineralogy to be largely representative of that at the time of sedimentation.

Clay mineralogy was determined by using X-Ray Powder Diffraction (XRD) at Louisiana State University using a Panalytical Empyrean X-Ray Diffractometer. Forty selected samples within the MTC were soaked in water until there was no flocculation, with Na_3PO_4 added to de-flocculate when necessary. Samples were centrifuged for separation of the <2 µm material. Four XRD patterns were generated from each oriented sample smear. The first pattern was collected from the sample in air-dried conditions. The second XRD pattern was generated from a glycolated sample after the slide was then placed in a desiccator with ethylene glycol for a minimum of 8 h at 25°C. t. The third and fourth XRD datasets were collected after the sample was subjected to heat treatments of 300°C for 1 h, and then 550°C for 1 h, respectively. XRD analysis began immediately after glycolation, and immediately after the first heat treatment. In this study we use the semi-quantitative method of Biscaye (1965) to estimate the clay assemblage, which is based on peak-intensity factors determined from calculated XRD patterns as measured by MACDIFF software. For clay minerals present in amounts >10 wt% uncertainty is estimated as better than ±5 wt% at the 95% confidence level. Uncertainty of peak area measurement based on repeated measurements is typically <5%. Data are presented as relative concentrations of the total clay assemblage in Table 5.

DEFINING THE TOP AND BASE

Microfossil assemblages within the sediments provide constraints on the age of emplacement. The oldest sediment overlying the MTC was dated at around 10.8 Ma based on nannofossil assemblages and paleomagnetic stratigraphy (Pandey et al., 2016c). In Hole U1456D the first appearance of *Discoaster hamatus* (10.55 Ma) marks the top of Zone NN8 (Pandey et al., 2016a), while in Hole U1457C the interval 859.49–995.93 mbsf contains *Catinaster coalitus,* which has a total age range of 9.69–10.89 Ma (Pandey et al., 2016b). The presence of *Discoaster bellus* (first appearance at 10.40 Ma) within this interval also constrains the age to between 9.69 and 10.40 Ma. Much of the interval from 1009.21 to 1054.34 mbsf at Site U1457 contains a mixture of different nannofossil species.

Above the MTC ~~there is~~ a coherent assemblage of nannofossils suggestive of hemipelagic sedimentation and not the mixed assemblage of early Neogene and Paleogene forms found within the MTC, as might be associated with a reworked deposit. We use this noticeable change in nannofossil assemblage as a criteria for defining the top of the MTC. In this study we define both a sedimentary and biostratigraphic top from the core, as well as the top inferred from the strong reflector in the seismic image, typically associated with massive carbonate beds. The sedimentary top of the deposit marks the transition from sediment that is clearly slumped or tilted in the core and appears to have been affected by syn-sedimentary deformation (Figs. 3 and 4) while the biostratigraphic top represents the transition from reworked into pristine nannofossil assemblages. The difference in depth, ~35 m, is significant and could represent continued slumping and reworking of young sediments after the initial emplacement of the main MTC bodies.

The base of the complex is easily established in both drilling sites, being marked by the presence of carbonate breccias immediately overlying fine-grained sediments (Figs. 3 and 5). The depth of this contact is 1101.65 and 1054.1 mbsf at Sites U1456 and U1457, respectively. A key observation is that in the thicker Site U1456 section there is a 20-m-thick interval in which normal hemipelagic sedimentation was briefly reestablished, based on the lack of reworking in the nannofossil assemblages. This spans from around 956 to 935 mbsf (Figs. 3 and 6). This shows that the MTC must have been emplaced in at least two phases separated by a pause, despite the fact that this is not apparent in the seismic image. What is surprising is that the top of this hemipelagic hiatus in mass wasting is not marked by a fresh influx of clearly reworked brecciated carbonate material. Much of the hemipelagic interval comprises massive or parallel-laminated mudstones with a couple of medium-bedded to massive sandstones representing less than 10% of the section (Fig. 6A). This is only moderately different from the material which lies above the hemipelagic layer that is characterized by mudstones interbedded with thin beds of siltstone. Above the hemipelagic layer, however, there is clear evidence for slump folding, tilted bedding and microfaulting, which testifies to the redeposited character of these sequences, as well as the mixed nannofossil assemblage. ~~It is only in the somewhat shallower part of the section at Site U1456 there is~~ evidence for a fresh influx of very coarse redeposited carbonate debris flow material, above 874.2 mbsf (Fig. 3A).

At both sites, the topmost part of the deposit largely comprises fine-grained, bioturbated claystones and clay-rich siltstones that are otherwise hard to distinguish from the background deposits of the Indus submarine fan, especially when they are not deformed. Tilted bedding is suggestive of deformation but might be interpreted as being coring related. The presence of slump folds close to the sedimentary top of each drilled section is, however, more conclusive in demonstrating continued mass wasting above the coarser grained basal units.

SEDIMENTARY FACIES

The sedimentary facies within the MTC were determined on the basis of core descriptions and, in particular, the analysis of sedimentary structures that give clues to the depositional processes that were operating during emplacement. We here describe the major sediment types and provide interpretations of the depositional mechanisms. These are summarized in Figure 3.

Limestones

Short intervals of the MTC comprise coherent sections of fine-grained limestone that show little evidence for the action of high energy reworking depositional processes. Limestones are found at Site U1456 within the lower part of the section around 1050 mbsf depth (Fig. 3). The limestones are typically massive and generally fine-grained micrite with moderate amounts of clay that give them an off-white color. Heavily bioturbated sediment with vertical *Zoophycos* trace fossils are typical of sedimentation in moderately deep water, often close to the shelf edge (Fig. 7A)(Ekdale et al., 1984; Seilacher, 1967). Figure 7B shows a massive micritic limestone with some evidence of bioturbation, but which indicates minor recrystallization along stylolites, highlighted by thin clay-rich partings. Neither deposit contains indication of strong current activity, such as ripples or laminations, or even a well sorted granular texture, but rather sedimentation in a low energy carbonate-rich environment probably below storm-wave base (<40 m)(Peters and Loss, 2012). Short intervals of limestone are also found at Site U1457 very close to the base of the MTC ~1050 mbsf. These are granular and porous and may be the product of higher energy sedimentation in relatively shallow water depths (<30 m). Again, the limestones are tan-colored rather than being pure white that is indicative of a modest clay content. Given the modern significant water depth (3523 m at Site U1457) we propose that these limestones represent coherent blocks of relatively shallow water material that were emplaced as part of the brecciated units near the base of the MTC.

Carbonate Breccia Debrites

The vast majority of the carbonate sediment in the MTC are breccia clasts found mostly in the bottom part of the deposit at Site U1456 (970–1101 mbsf), with further yet more limited clasts in the upper part of the MTC at the same site. They are also found immediately above the base of the MTC at Site U1457 (Fig. 3). These breccias are thick-bedded, ranging close to 20 m thick for individual beds separated by finer grained units. At Site U1456 there are multiple such breccia units, stacked on top of each other, that are preferentially developed towards the base of the sequence. The breccias are sometimes overlain by calcarenites (described below) or by mudstones with a sharp boundary between the two lithologies. The breccias are extremely poorly-sorted and the individual clasts are angular to sub-angular. Clast size ranges up to and greater than the width of the core (>10 cm). There is usually no trend towards fining or coarsening upwards within individual units, although one coarsening upwards sequence is seen in Section U1456D-43R-1 (860 mbsf). The fabric of the sediment is rarely clast-supported (Fig. 8A) but is normally suspended in a dark muddy matrix (Fig. 8B).

The limestone clasts are pale tan to bright white with the interior showing a very fine-grained or slightly granular sediment classified as micrite or more rarely packstone and wackestone (Dunham, 1962). In the part of the section densest in limestone clasts (~1036 mbsf at Site U1457), clasts are seen to indent one another both in core surfaces (Fig. 8A), as well as in microscope thin sections (Fig. 9D). We interpret this as a result of dissolution during diagenesis and burial.

The vast majority of the carbonate rocks redeposited in the debris flows appear to have been lithified prior to their resedimentation. In combination with the observation of angular clasts, we see coherent rafts of sediment (>10 cm width) floating within finer grained material (Fig. 8B). There is some evidence that some of the carbonate sediment was not lithified during emplacement because soft sediment folding of the deposits, such as seen in muddy limestones (Fig. 10A) can be observed. However, these deformed deposits only represent a relatively small part of the total sequence. ~~It is clear that~~ brittle deformation is important locally, especially between and within the more coherent carbonate blocks. Slickensides especially testify to rapid brittle deformation of the carbonate rocks during their emplacement (Fig. 8C). Most of the debris flow units are extremely poorly-sorted but sometimes are represented by coarse sandstones devoid of larger clasts (Fig. 8D). In these, larger granular clasts are supported in a muddy sandstone matrix with no clear grading within the unit.

Although limestone fragments dominate the debris flows, it is noteworthy that in places there is evidence for reworking of volcanic rocks into the flows (Fig. 10B). These clasts are weathered red-brown and are sub-rounded. The largest single clast was found at 879 mbsf at Site U1456 within a poorly indurated conglomeratic part of the debris flow sequence. The clast is an 8-cm-wide fragment of vesicular aphyric basalt that is presumed to be derived by erosion from the Deccan Plateau volcanic sequences exposed across peninsular India. The clasts were likely eroded on to and then reworked across the continental shelf because being redeposited in the MTC.

The limestone, from which the carbonate clasts were derived, formed as a typical shallow-water deposit in a biologically productive zone mostly starved of clastic sediment input. Original water depths were within the photic zone on the continental shelf or within a back-reef setting (<50 m), with only moderate amounts of current activity, since we see no evidence for strong sorting or high energy deposits such as oolites or grainstones (Dunham, 1962). These original rocks have mostly been broken and reworked as debris flow deposits during the emplacement of the MTC. The muddy matrix has a separate provenance, either from the deep-water slope of peninsular India or from the Indus Fan itself, as discussed below.

Calcarenites

Calcarenite is present in each carbonate section, in the form of massive, well-sorted units suggestive of high energy current transport. Beds of calcarenite are several meters thick and generally massive and structureless, although they can develop a sub-horizontal fabric suggestive of current flow. Where the deposits are finer (Fig. 10D), there is a shear-type fabric developed within the calcareous siltstones. In the coarser grained units (Fig. 10C) there is some evidence for internal soft sediment deformation, although generally the units are homogenous and comprise uniform, gray, coarse-grained sandstone. They are well-sorted and clast-supported, with very little muddy matrix, suggestive of a high energy depositional regime. The majority of the clasts are carbonate, although there are a significant number of dark grains of organic carbon origin. These calcarenites often have sharp tops that are interpreted to reflect erosion of the deposit prior to the emplacement of overlying units. Figure 10D shows a calcareous siltstone sharply overlain by conglomeratic sandstones deposited as debris flows. Very few sedimentary structures are seen within these deposits, so that we infer sedimentation in an upper flow regime resulting in relatively laminar deposits without any current ripples or finer interbeds. Sediment concentrations are inferred to have been very high during deposition, which terminated rapidly.

Turbidites and Hemipelagic Mudstones

Apart from the carbonate-dominated debris flows, minor turbidite sandstones and dominant siltstones and mudstones make up the largest part of the MTC. These are also interbedded with associated hemipelagic mudstones. In the coarsest sandstones, each turbidite shows a classic fining upward sequence (Fig. 11A), with largest carbonate fragments suspended in a dark clastic mud matrix. Locally, there are sub-horizontal lamination although sedimentary structures are poorly developed, with up-section fining dominating characteristic of these deposits. In the upper parts of the MTC at both sites, muds show lamination and interbedding of modest amounts of muddy silt (Fig. 11B). Elsewhere, the deposits are massive, dark gray mudstones with few sedimentary structures. These contrast with the draping mudstones that overlie the catastrophically emplaced MTC where typical deep-water trace fossil assemblages (i.e., *Zoophyco*s;(Fig. 11C) characterize the hemipelagic sedimentation and eliminate the possibility of large-scale mass wasting. This is in contrast to the muddy upper sections of the MTC itself, where there is evidence for laminar current flow that follows the initial emplacement of the carbonate debris flow deposits at the base of each cycle. In general, the grain sizes are relatively limited, with only few a thin-bedded sandstones and occasional siltstones developed within what is otherwise a dominantly (95%) muddy sequence. Distinguishing muddy sediment with the MTC from the hemipelagic interval within Site U1456 is difficult without the help of micropaleontology evidence.

Syn-sedimentary deformation within the muddy turbidities include folds, micro-faults, and tilted bedding (Fig. 11D) and are particularly easy to see in well-laminated sequences. Dip of lamina can be high (>50°), indicating significant deformation of the muddy units after sedimentation. In addition to ductile structures, there is evidence for compressional reverse faulting. Significant dips and deformation are evidence for incorporation as part of the MTC rather than the subsequent hemipelagic sedimentation of the Indus Fan, which is only gently inclined like the seafloor or the top of the MTC (~1.2˚ according to Calvès et al. (2015)).

Micro-Facies

Petrographic analysis can be used to help interpret paleoenvironment and depositional mechanisms from facies identified in the cores. Figure 9A shows a silty laminated mudstone from the upper part of the MTC at Site U1457 that is interpreted here as a turbidite deposit. The massive calcarenite beds that overlie debris flow conglomerates are ~~seen to be~~ relatively poorly sorted and matrix supported, at least in places, in thin section (Fig. 9B). Clasts are rarely composed of calcite crystals but are dominated by a variety of finer limestone facies, especially micrite. Aggregates of dolomite crystals ~~are observed~~ (Fig. 9C) ~~and~~ interpreted to represent diagenetic alteration of original calcite via interaction with magnesium-rich waters prior to resedimentation. Their presence is suggestive of redeposition from shallow water areas where this mineral generally forms.

There are large numbers of microfossils and their fragments within the breccia limestone clasts. Foraminifers are abundant (Figs. 12A, 12B, 12F). In addition, we also confirm the presence of crinoid fragments (Fig. 12D), bryozoans, and rare radiolarians (Fig. 12E). The skeletal assemblage of most limestone clasts is dominated by calcareous red algae and benthic foraminifera (including both miliolids and large rotaliids; Fig. 12C). Rare echinoderms, mollusks and hermatypic coral fragments are also present. Some skeletal grains, originating from a shallow-water environment (coralline algae, large echinoid spines, large benthic foraminifera), also occur within the matrix (Figs. 12H, 12I). The occurrence of what is likely to be *Lockhartia*, together with the peyssoneliacean red-alga *Polystrata alba*, suggests that at least part of the eroded limestone was of Paleogene age (Fig. 12C)(Bassi and Nebelsick, 2000; BouDagher-Fadel, 2018). The matrix is largely dominated by planktonic foraminifera with minor contribution from small rotaliids (Figs. 12G).

These characteristics suggest that the MTC involved both lithified inner platform deposits (the source of limestone fragments) and outer platform deposits still composed of loose grains (the source of the muddy matrix with planktonic foraminifera).

DEPOSITIONAL MECHANISMS

Most sediment within the MTC are either debris flow deposits, well-sorted calcarenites, or dominantly clastic turbiditic siltstones and mudstones. Both phases of the MTC at Site U1456 (Fig. 3) show large-scale fining upwards cycles, with a dominance of carbonate debris flows towards the base grading into more siliciclastic turbidite sedimentation towards the top. Smaller, shorter phases of fining upwards cycles are further observed within the two overall fining upwards cycles at Site U1456. For example, the upper part of Phase 1 (Fig. 3), comprises a basal unit from between 999.2 and 984.0 mbsf that is dominated by rafted carbonate sheets and carbonate debris flow material (Figs. 3 and 6B). This interval is likely a second pulse after the initial Phase 1 event. Above 984.0 mbsf there is a transition to massive thick-bedded calcarenite with slump folds, although this is truncated sharply at 973 mbsf by mudstones that rapidly transition into the hemipelagic sediment described above (Fig. 6B). This implies that the basal Phase 1 unit, especially at Site U1456 comprises a series of pulses rather than one single gigantic deposit as might have been implied by the seismic data alone (c.f.(Calvès et al., 2015)(Fig. 2).

The base of Phase 1 at both sites is characterized by a thick-bedded sequence of debris flow calcareous breccias and rafts of undeformed shallow water carbonate (Fig. 5). These are not surprisingly the thickest such deposits within the entire drilled section. Although Site U1456 is in a more central location within the basin, the oldest debris flow breccia at the base of Phase 1 is thinner in this location than at Site U1457 and transitions more rapidly up into thick-bedded breccia and interbedded calcarenites. Both sections, however, do show an overall fining upward between the base and overlying mudstone units. The initial debris flow sedimentation appears to be ~94 m thick at Site U1456 (1101.6–1007.2 mbsf) and ~48 m thick at Site U1457 (1006.4–1054.3 mbsf; Figs. 3 and 5).

In general, calcarenites alternate with debris flow conglomerates (Fig. 5A) indicating alternating depositional mechanisms within a single emplacement episode. Individual debris flow events are followed by high energy upper flow regime periods of sedimentation where massive well-sorted calcarenites were deposited before being followed by another debris flow unit. However, presumably all this material was emplaced over a relatively short period of time. The carbonate-dominated debris flows form the initial erosive base of the MTC, followed by mud-dominated turbidite sedimentation and hemipelagic fallout representing the tail of the MTC. At Site U1456 this sequence is then repeated after the hemipelagic break. Soft sediment deformation is commonly seen in the more laminated sections indicative of slumping after sedimentation. It seems unlikely that poorly consolidated mudstones and siltstones could have been emplaced hundreds of kilometers in a semi-coherent form, unlike the well-lithified limestone clasts seen close to the base of each section.

GEOCHEMISTRY

Bulk Geochemistry

We use a CN-A-K ternary diagram to illustrate major element geochemistry of MTC samples compared to sediments from the Indus Canyon and delta. The sediment from the MTC largely plots within the range of the Indus Canyon and trends towards higher values of Al_2O_3 (Fig. 13A). MTC samples appear to have higher values that trend towards the illite end-members and may be more depleted in biotite and feldspars compared to the delta. This is likely a result of sediment transport, similar to what has been observed in the Indus Canyon (Li et al., 2018).

Sediments in the muddy upper part of the MTC at Site U1457 largely plot with low Chemical Index of Alteration (CIA), which is a proxy of the state of weathering of a sediment compared to pristine bedrock (Nesbitt et al., 1980). The muddy upper MTC samples trend more towards the Quaternary Indus Delta field compared to the lower parts of both Phase 1 and Phase 2, which show more overlap with western Indian Shelf sediments, largely derived from rivers draining the Deccan Plateau (Kurian et al., 2013). This plot implies that the upper muddy sediments at Site U1457 had a dominant source from the Indus River/Fan and little inputs from western peninsular India.

The sediment in the MTC can also be characterized using other major element discrimination diagrams. Figure 13B shows the scheme of Herron (1988) in which the Phase 1 and Phase 2 samples largely plot within the Fe shale field, with a few slightly depleted in Fe and plotting as shales. Again, we plot these samples along with the western Indian Shelf, Indus Canyon and delta sediments. Samples from the upper muddy top to Phase 1 at Site U11457 form a cluster within the range of the Indus Canyon sediments, suggesting a dominant provenance of reworked Indus material. Comparison with sediment from the western Indian shelf shows a significant difference, with the shelf sediment typically plotting with much higher Fe contents, similar to the lower Phase 1 and 2 sediments. We infer that the bulk of the sediment in the lower MTC comprises mostly Indian margin sediment with muddy top dominated by sediment eroded and redeposited from the Indus Fan.

Nd and Sr Isotopes

We use Sr and Nd isotope values to constrain the provenance of siliciclastic sediment in the MTC. By cross-plotting Nd and Sr isotopic compositions from source regions such as the Deccan Traps, peninsular Indian rivers, Transhimalaya, Karakoram, Greater Himalaya, Kirthar and Sulaiman Ranges, and modern/Quaternary Indus-derived sediment allows the origin of the sediment to be further constrained (Fig. 14). This diagram shows that the MTC samples form a relatively discrete cluster with one exception that has especially positive ε_{Nd} values that fall within the Deccan and Transhimalayan arrays. When we compare these data with potential sources, it is clear that the bulk of the sediments lie within the isotopic range defined by the Indus submarine fan sediments at the same drilling sites (Clift et al., 2018). This is consistent with the argument that much of this material may be reworked Indus-derived sediment. However, we note that it is impossible to exclude mixing of sediment from the peninsular Tapti or Narmada Rivers. The isotope compositions by themselves do not allow us to quantify the degree of reworking from these sources as they are similar to the Indus. Although the MTC samples plot with higher ε_{Nd} values compared to the Quaternary Indus Canyon, as well as the Kirthar and Sulaiman ranges, such a composition could largely be explained through temporal variation in the Indus River itself (Clift and Blusztajn, 2005; Clift et al., 2018). The one very positive ε_{Nd} sample is anomalous and plots with even more positive values than the Tapti River. This is strongly suggestive of erosion from peninsular India and is corroborated by the presence of vesicular Deccan Plateau basalt fragments as previously noted.

We can look at the stratigraphic variation in isotopic compositions through time at both sites (Fig. 15). In both cases, Nd isotope compositions plot within error of the Quaternary Indus or with slightly more positive ε_{Nd} values. We note that the most positive ε_{Nd} values in each borehole are found within the debris flow conglomerate units bearing basaltic clasts at the base of the lower part of the MTC. This is especially true at Site U1456 (Fig. 15A). Variations in $^{87}Sr/^{86}Sr$ also mirror this general evolution.

The provenance of the coarse-grained carbonate debris flow deposits is different from those of the finer grained sediments overlying them. The fine-grained sediments may represent recycling of pre-existing fan sediments into the top of the MTC, while the debris flow deposits are more closely associated with mass wasting from the western Indian continental margin. It is possible that some Indus River sediment could have been transported east along the shelf, carried by longshore currents from the river mouth, and deposited offshore Saurashtra before being redeposited as part of the MTC. However, there is no evidence that significant Indus sediment travels farther east than the Rann of Kutch (Khonde et al., 2017; Kurian et al., 2013). The simplest interpretation is that the upper muddy layers of the MTC represent entrained and reworked Indus Fan material.

Heavy Mineral Analysis

The heavy-mineral assemblages help to constrain the source area of the MTC. The concentration of heavy minerals in all samples is very low suggesting a strong depletion due to intrastratal dissolution of unstable silicates (Garzanti, 2017). Consequently, a relative enrichment of ultrastable minerals is observed (ZTR index of Hubert (1962)). The two samples (U1456E-15R-1W, 61-63 cm and U146E-17R-4W, 131-133 cm), analyzed from the carbonate breccia present extremely low HMC (0.04–0.05%) with common augitic clinopyroxene (~6%) and rare spinel (2–3%). The minerals also show corroded surficial textures, indicating a strong diagenetic overprinting (Ando et al., 2012). A similar fingerprint is detected in Sample U1456E-7R-1, 80-82 cm where green and brown augite are abundant (48%). In all these samples, ~~there are~~ common garnets associated either with apatite, titanite, epidote, zircon, tourmaline, and metamorphic Ca-amphiboles, potentially derived from recycled sediments from the Himalaya-derived Indus Fan turbidites eroded by the MTC. Notwithstanding diagenetic dissolution, the highly unstable augitic clinopyroxene (volcanic origin) always dominates over metamorphic amphiboles, suggesting a sizable contribution to the MTC from the Indian passive margin, and especially from Deccan Plateau basaltic lavas. Sample U1456E-4R-1W, 110-111 cm is a calcarenite within which hydraulic sorting and high-energy currents preferentially selected the available heavy minerals suite derived from the MTC, concentrating platy heavy minerals such as chloritoid, Ca-amphiboles and tourmaline (lighter). The sample is partially depleted in denser garnet. This assemblage is completed with the presence of abundant apatite, common titanite, epidote and spinel with trace of kyanite, andalusite and staurolite.

Sample U1457C-88R-4W, 58-60 cm was deposited far from the Indian Passive margin and the mineralogy reflects a dominant contribution from recycled minerals derived from the erosion and re-deposition of the Indus Fan turbidites. The tHMC is very low (0.08%), and mineralogy is dominated by abundant epidote and garnet with common apatite and titanite. Ca-amphiboles dominate over clinopyroxenes, with a ratio 8:1, pointing to a major contribution from the Indus River and the Himalaya in this sample. The assemblage also includes tourmaline, zircon, chloritoid, Cr-spinel and trace of and kyanite, staurolite and andalusite.

The modern Tapti River was analyzed close to its mouth. The sample contains a very rich assemblage of heavy minerals (tHMC 17%) with dominant augitic clinopyroxenes (92%) and subordinate amount of metamorphic heavy-mineral, Ca-amphiboles, epidote, garnet and sillimanite. This mineralogical signature differs from the observed suite of orogenic heavy minerals observed in the modern Indus River and his delta (Garzanti et al., 2005).

The heavy mineral assemblage in the MTC and the very low concentration of heavy minerals points to different sources for the siliciclastic sediments, i.e., partially derived axially from the Himalayas via the Indus River (especially at Site U1457C) and partially derived transversally from the Indian peninsula (especially at Site U1456).

Zircon U-Pb Ages

To further constrain provenance, we compare detrital zircon U-Pb ages with existing data from the Indus river mouth (Clift et al., 2004), Indus Fan turbidites above and below the MTC (Clift et al., 2018), and with bedrock data from potential sources in the river catchment (Fig. 16)(DeCelles et al., 2000; Gehrels et al., 2011). Although the zircon ages from source bedrock overlap with each other, each source regions demonstrates strong preferential age spectra that can be used to discriminate between them. Zircons from Nanga Parbat, Kohistan, the Transhimalaya, and the Karakoram generally have younger ages (<300 Ma) than those from the

Himalayan ranges (Alizai et al., 2011)(Fig. 16). Both the Greater and Tethyan Himalaya have U-Pb age peaks at 300–750 Ma and 750–1250 Ma, with older ages at ~1850 Ma characterizing the Lesser Himalaya

The volume of sample available for U-Pb dating from Core U1457C-7R (the only suitable sediment seen in the MTC) was extremely limited such that only 51 grains yielded concordant ages, which is somewhat lower than the 113 minima suggested by Vermeesch (2004) for a sample with complex provenance. Nonetheless, some inferences concerning provenance can be made. What is clear is that young ages dominate with 17 grains dated at less than 100 Ma (Fig. 16). The age spectrum bears most similarity with Indus Fan turbidites dated at 7.8, 8.3, and 15.6 Ma, but all are in contrast with the ages from the modern river. The match between these young grains and sources in the Karakoram and Kohistan argue for the sand to be an Indus-derived sediment and not from sediment transported from the Indian peninsula where zircon ages are Paleozoic or typically much older. This conclusion is consistent with the Nd and Sr isotope data from the upper parts of the MTC. The analyzed sandstone was sampled below the sediment/structurally defined top of the MTC but above the carbonate-dominated debris flow facies at the base of the complex, i.e., within the muddy but slumped top of the MTC. This implies that the upper parts of the MTC are Indus Fan sediments entrained in the tail of the MTC during emplacement.

Clay Mineralogy

The clay mineral assemblages within the MTC can be used to assess provenance by semiquantitative analysis and comparison with existing data from other sources. When plotted on the ternary diagram of (illite+chlorite), kaolinite, and smectite (Fig. 17) there is significant overlap between the new MTC data and other Arabian Sea sediments (Rao and Rao, 1995). In general, the MTC clays are low in kaolinite and form an array between the smectite and (illite+chlorite) end members. In this respect, they show a similar character to sediments from the Indus fan and have significant overlap with Quaternary clays from the Indus Canyon (Li, 2018). Samples from Phase 1 of the MTC have very high smectite contents, similar to the Paleocene sediments overlying basement at Site U1457, suggestive of a volcanic source. They are close to sediments recovered from the inner shelf offshore Saurashtra and from the Gulf of Cambay. Phase 2 sediments and the hemipelagic layer are slightly less smectite rich but overlap with the Holocene Indus Shelf, as well as some modern Indian Shelf sediments. We note that the bulk of the muddy upper Phase 1 sediments plot with higher (illite+chlorite) values and they also tend to have slightly higher kaolinite compared with analyses of sediments from the Indus floodplains (Alizai et al., 2012). These sediments are similar to the assemblage recognized from the outer Saurashtra margin (Rao and Rao, 1995) and are similar to many clay assemblages within Indus Fan turbidite sequences. Overall, the MTC deposits have lower kaolinite compared with most Western Indian shelf deposits but some samples plot closely to the shelf. It is also noteworthy that the MTC assemblages generally show lower (illite+chlorite) compared with many of the Miocene-Recent Indus submarine fan deposits, which likely indicates a mixed provenance of Indus and Indian peninsular sediment. However, because illite and chlorite are the product of physical weathering rather than chemical weathering their relatively high contribution to the MTC could also indicate reduced chemical weathering of fan sources since MTC emplacement. These data are consistent with a dominant recycling of Indus Fan deposits in the upper muddy parts of the MTC, but with greater involvement of clays derived from the Western Indian margin in the lower part, especially in Phase 1. The similarity with modern nearshore sediments offshore Saurashtra and Cambay is consistent with an origin in this part of the margin.

Clay mineralogy shows significant variation with depth (Fig. 15). At Site U1456 the carbonate-rich part of the section shows particularly high smectite contents and relatively low (illite+chlorite) values. Smectite only becomes less abundant than these two physically weathered clays above the upper Phase 2 carbonate debris flow unit. At Site U1457 the carbonate-rich part of the section similarly is smectite-rich, but immediately above this level the sediments become dominated by an (illite+chlorite) assemblage similar to the Indus Fan. It is noteworthy that the Paleocene sediments beneath the MTC at Site U1457 are ~100% smectite, possibly reflecting chemical weathering of the underlying basaltic basement. Clay mineralogy supports the Nd and Sr isotope compositions in showing a characteristic difference between the carbonate-dominated sections that indicate similarity to the western Indian margin, whereas the mudstone dominated sequences further upsection in the MTC are most similar to compositions associated with the Indus Fan.

SEDIMENT BUDGET

To assess the potential of sediment delivery rates and margin oversteepening as triggering mechanisms of the MTC, a sediment budget from the western Indian margin was generated using standard two-dimensional backstripping methods from seismic profile data (Clift, 2006; Kusznir et al., 1995). This was to primarily test the hypothesis that the rapid accumulation of sediment on the continental margin resulted in an unstable stratigraphy that was then more liable to mass wasting events like the Nataraja MTC. There is strong evidence that the Western Indian continental margin is gravitationally unstable as a result of the large-scale compressional thrusts seen in seismic profiles towards the base of the continental slope seen between the Saurashtra shelf and Bombay High (Fig. 1)(Calvès et al., 2015; Nair and Pandey, 2018). These features are often associated with slopes prone to gravitational collapse, which in this region, has yet to manifest in the dramatic fashion of the Nataraja MTC. In order to estimate the mass flux of the margin, we use the cross-margin seismic reflection profile of Nair and Pandey (2018)(Figs. 1 and 18). Their northernmost profile lies immediately south of the scarp region identified by Calvès et al. (2015) and which we consider to be potentially representative of the sedimentation in the source regions of the MTC prior to its redeposition. For the purpose of this study, we use the age control provided by Nair and Pandey (2018), at least for the continental shelf and slope areas (Fig. 18A). West of the toe of the slope sedimentation is linked to the Indus Fan and may not be representative of the mass flux to the Saurashtra Shelf. Figure 18A shows the interpretation of Nair and Pandey (2018) with a conversion from their seismic travel time scale to depth made on the basis of multichannel seismic stacking velocities derived from the Indus shelf, as used by Clift et al. (2002)(Table 6). We do this because of the absence of such data from the Saurashtra region itself. We prefer to use velocity data from the Indus continental shelf rather than from the deep basin because as the sediment thicknesses are much greater under the continental shelf, they are more comparable to those seen offshore the Indus River mouth. Based on the lateral variability in velocities seen on the Indus Shelf, we estimate that this conversion may introduce uncertainties as high as ±20% (Clift, 2006). Stratigraphic ages are then assigned numerical ages based on the timescale of Gradstein et al. (2012).

The depth-converted line was then backstripped using standard decompaction methods (Kusznir et al., 1995; Sclater and Christie, 1980). This was done to restore each dated sediment layer to its original thickness prior to burial. Knowledge of the sediment type is important to this calculation because shales experience much greater loss of porosity during burial than do sandstones (Sclater and Christie, 1980), and in this case, we used lithological data from Wandrey (2004) and Rao and Talukdar (1980). These studies show a mixed Cenozoic sequence dominated by silty muds and carbonates offshore Saurashtra. The decompaction process involves accounting for the loss of porosity of the sediment during burial, which would otherwise result in an underestimation of deposited volumes for the older, deeper buried sediment packages. After the original, uncompacted volume of sediment in each dated interval has been determined, the mass of rock delivered during that time period can be calculated. Errors in lithology and compaction history are much smaller than the time-depth conversion and rarely exceed 5%.

In this study two-dimensional decompaction was calculated using the program *Flex-Decomp*™ (Kusznir et al., 1995). It must be assumed that the analyzed profile is representative of the total mass flux to the margin since rifting of the Arabian Sea ~66 Ma (Bhattacharya et al., 1994). Because we only have one profile close to the area of mass wasting, and no estimate of the total sediment mass offshore Saurashtra, it is not possible to make a volume calculation. However, the two-dimensional budget does at least allow us to estimate the volumes of sediment delivered per kilometer of margin close to the source of the MTC. Our results show a clear trend to increasing mass flux after 26 Ma (Fig. 18B), with a peak between 16 and 11 Ma. Because the resolution of the budget is constrained by the presence of the dated horizons, it is not possible to accurately say when the peak sediment flux was achieved, but this analysis confirms that the Middle Miocene was a time of rapid sedimentation offshore Saurashtra, a pattern that it shares with many other Asian delta systems. As a result, it seems likely that the pulse was caused by faster erosion driven by heavy summer monsoon rains (Clift, 2006). We suggest that much of the gravitational instability on the western Indian margin was caused by rapid sedimentation in the

Middle Miocene causing oversteepening of the shelf edge, comprising large thicknesses of sediment liable to incomplete dewatering during burial. The reducing sedimentation rates after 11 Ma may explain why a second such slide has not been emplaced in this part of the margin.

SEISMICITY

As well as an over-steepened continental margin caused by increased sediment flux, we investigate the possible triggering of the MTC as a result of seismic activities that are often implicated in the emplacement of large mass wasting complexes (Kastens, 1984). Figure 1 shows the location of earthquakes greater than 4.5 magnitude since 1960 in the vicinity of the source region for the MTC. ~~There is~~ some seismicity related to the plate boundary west of the Indus delta and there are small amounts of activity in the Saurashtra Peninsula itself, immediately opposite the scar in the continental shelf. It is apparent that the greatest concentration of seismic activity is however around the Rann of Kutch, where historic intraplate events up to 7.7 magnitude have been recorded (Bilham, 1999). This activity reflects reactivation of earlier rift-related faults due to compression linked to the India-Eurasia collision (Bilham et al., 2003; Biswas, 2005). This part of the Indian plate is a weak zone and may well have been active as a seismic hotspot for significant periods of time. We suggest that ~~it is~~ the relative proximity of the Saurashtra margin to this tectonic feature (<300 km) ~~which~~ may have initiated the mass wasting in that region, rather than further south along the margin where sediment flux was also high.

SYNTHESIS AND CONCLUSIONS

This study~~, made possible through drilling,~~ reveals for the first time the internal structure and origin of the Nataraja MTC, and extends our understanding based on the earlier seismic surveying of the deposit. At Site U1456, there is clear evidence that the MTC was emplaced in two major phases separated by a significant break (Fig. 19). Even the larger, earlier Phase 1 can be broken down into at least two stages, indicative of pulsed emplacement. The basal part of each drilled section of the complex comprises debris flow carbonate breccias and larger rafts of shallow water limestone, which can be traced back to collapse of the carbonate edge of the continental shelf offshore Saurashtra. The MTC is emplaced as a number of fining upward sequences with debris flow breccias, overlain by well sorted, coarse calcarenite deposited by high velocity currents following in the wake of the initial mass wasting landslide. These are overlain by muddy and turbiditic deposits, which are increasingly siliciclastic in character. At Site U1457, only a thinner section of the earlier Phase 1 appears to be preserved, but a second Phase 2 is apparent at Site U1456. Again, there was an emplacement of carbonate-rich debris flows, although these were preceded and followed by muddy turbidite deposits, largely reworked from pre-existing sediments of the Indus Fan. The top of each drilled sequence shows a separation between sediment where the biostratigraphy is mixed and where slumping continues to occur in the aftermath of the original depositional event.

Nd and Sr isotopic data, together with heavy-mineral assemblages, show that the siliciclastic fraction of the deposit is associated with the western Indian continental margin, at least in the debris flow part of the deposits although the overlying muddy turbidite units share the same characteristics as the Indus submarine fan and suggest entrainment of sediment already deposited in Laxmi Basin in the wake of the carbonate-rich debris flows that formed the MTC in the first place. Limited zircon data at Site U1457 also show the clear signature of the Indus River, although this applies only to the muddy units overlying the carbonate debris flows. We envisage that enhanced sediment delivery to the western Indian continental margin driven by strong monsoon during the middle Miocene resulted in an oversteepened continental margin that was in a gravitationally unstable state. Exactly what triggered the collapse is not clear, but may well be related to seismic activity in the nearby Rann of Kutch where large earthquakes continue to the present day. Compressional deformation structures in the western Indian continental margin south of Saurashtra suggest that this region too is in a compressional and potentially unstable situation. However, decreasing sediment flux to the continental margin since the middle Miocene has lessened the instability of the continental slope and reduced the chance of mass wasting, especially further south away from potential seismic triggers. The western Indian margin, however, has also experienced the increasing sedimentation rates linked to the onset of northern hemisphere glaciation and so the potential for significant geohazard still exists. Nonetheless, the fact that there has been no similar large event since 10.8 Ma does argue for this being relatively low risk at the present time.

Acknowledgments

This work was made possible by samples given by International Ocean Discovery Program. Project funding came from the Charles T. McCord Jr Chair in Petroleum Geology at LSU. We thank Alan Roberts and Nick Kusznir for use of FlexDecomp software.

Figure Captions

Figure 1. A) Shaded topographic and bathymetric map of the Arabian Sea showing the location of the core sites discussed in this study (yellow dots). Base map from GeoMapApp. Dashed yellow lines show proposed continent-ocean boundaries. Dashed white lines show oceanic transform faults. Numbered red circles indicate existing scientific boreholes from Deep Sea Drilling Project (DSDP) and Ocean Drilling Program (ODP). Pink squares show major cities. Magnetic anomalies (thin gray numbered lines) are from Miles et al. (1993). Green-filled circles show earthquakes >4.5 magnitude since 1960 recorded by US Geological Survey. B) Close-up map of Laxmi Basin showing the precise location of the drill sites. A pink dashed line shows the extent of the Nataraja MTC (Calvès et al., 2015). Light blue lines show locations of seismic profiles shown in Figure 2.

Figure 2. Seismic profiles of the core sites (left) with interpretation (right) showing the mass-transport complex in the immediate vicinity of (A) IODP Site U1456 and (B) IODP Site U1457. Modified from Pandey et al. (2016c). See Figure 1 for locations of lines.

Figure 3. Summary stratigraphic columns showing the lithologies and interpreted facies of the mass-transport complex at (A) IODP Site U1456 and (B) IODP Site U1457. Black shading in second column indicates recovery, with white showing lost section. mbsf = meters below seafloor.

Figure 4. (A) Sedimentary log showing the top of the deposit, U1456D-33R to U1456D-42R; (B) Sedimentary log showing the top of the deposit, U1457C-69R to U1457C-78R. Black shading in

second column indicates recovery, with white showing lost section. mbsf = meters below seafloor.

Figure 5. (A) Sedimentary log showing the bottom of the MTC, U1456E-16R to U1456E-19R; (B) Sedimentary log showing bottom of the MTC, U1457C-86R to U1457C-92R. Lithological patterns and sedimentary structures same as Figure 4. Black shading in second column indicates recovery, with white showing lost section. mbsf = meters below seafloor.

Figure 6. (A) Sedimentary log showing the deposit above and within the hemipelagic layer, U1456D-50R to U1456D- 53R. As shown, soft sediment deformation occurs until pelagic layer begins; (B) Sedimentary log showing the second pulse of carbonate debris flow material, U1456D-56R to U1456D-61R. Lithological patterns and sedimentary structures same as Figure 4. Black shading in second column indicates recovery, with white showing lost section. mbsf = meters below seafloor.

Figure 7. (A) Limestone with burrows (20 cm long), U1456E-12R-1, 42-47 cm (1045 mbsf); (B) Stylolite in limestone, U1456E-10R-3, 30-40 cm (1030 mbsf). Vertical scale is in cm below the section top. See locations on Figure 3.

Figure 8. (A) Coarse carbonate breccia with mudstone matrix, U1457C-90R-2, 75-83 cm (1036 mbsf); (B) Debris flow conglomerate with faulted mudstone raft (larger faults shown with white lines), U1456E-9R-4, 78-88 cm (1021 mbsf); (C) Core photograph of slickensides on a fault within silty claystone, U1456E-9R-4, 37-51 cm (1021 mbsf), (D) Coarse sandy, calcarenite,

U1457C-88R-5, 38-48 cm (1022 mbsf). Vertical scale is in cm below the section top. See location on Figure 3.

Figure 9. Thin section plane polarized photomicrographs of (A) Laminated sandy siltstone with quartz grains, U1457C-85R-1, 22-26 cm (997 mbsf). Note the finer muddy center of the image and the poorly sorted silt interbeds on either side with dominant quartz clasts; (B) Calcarenite, U1456D- 60R-1, 13-17 cm (1006 mbsf); (C) Euhedral calcite/dolomite crystals within larger grain, U1456E-15R-1, 12-16 cm (1073 mbsf); (D) Suture grain contact of carbonate clasts in breccia, U1456D-45R-4-52-57 cm (870 mbsf). See location on Figure 3.

Figure 10. (A) Slump folded calcareous siltstone, U1456D-58R-2, 43-53 cm (989 mbsf); (B) Deccan vesicular basalt clast, U1456D-46R-1, 16-25 cm (879 mbsf); (C) Massive calcarenite with ductile folded layer U1456D-41R-3A, 114-124 cm (841 mbsf); (D) Sharp contact between calcarenite and calcareous siltstone, U1457C-88R-7, 61-70 cm (1025 mbsf). Vertical scale is in cm below the section top. See location on Figure 3.

Figure 11. (A) Sandy siltstone showing gradual normal grading, U1457C-71R-3, 101-115 cm (865 mbsf) (B) Tilted, laminated turbidite deposit U1457C- 73R-2, 140-148 cm (881 mbsf); (C) Mudstone with *Zoophycos* burrows (one outlined for clarity), U1457C-68R-1, 42-52 cm (832 mbsf); (D) Steeply dipping laminated mudstone showing reverse faulting, U1456D-46R-3A, 139-148 cm (883 mbsf). Vertical scale is in cm below the section top. See location on Figure 3

Figure 12. Thin section plane polarized photomicrographs of (A) Uniserial benthic foraminifer in breccia clast, U1456E-15R-1, 12-16 cm (1072 mbsf); (B) Siltstone with planktonic foraminifers, U1456D-58R-2, 40-44 cm (989 mbsf); (C) Limestone clast with a specimen of *Lockhartia,* U1456E-17R-4, 131-133 cm (1086 mbsf); (D) Echinoderm spine in carbonate clast, U1456D-61R-2, 44-48 cm (1017 mbsf); (E) Foraminifer fragments in siltstone, U1456D-58R-2, 40-44 cm (989 mbsf); (F) Planktic foraminifers and bioclasts in carbonate breccia, U1457C-90R-1-6-10 cm (1034 mbsf). G) Planktonic foraminifer, U456E-7R-1, 80-82 cm (999 mbsf); H) Fragments of coralline algae (white arrows) included in the planktonic-foraminifer-dominated matrix; Plk = planktonic foraminifer, U1457C-88R-4, 58-60 cm (1021 mbsf); I) Orthophragminid fragment (white arrow) included in the planktonic-foraminifer-dominated-matrix; Dl = dolomite crystal, U1457C-88R-4, 58-60 cm (1021 mbsf). See locations on Figure 3.

Figure 13. (A) Geochemical signature of the analyzed samples illustrated by a CN-A-K ternary diagram (Fedo et al., 1995). CN denotes the mole weight of Na_2O and CaO* (CaO* represent the CaO associated with silicate, excluding all the carbonate (Singh et al., 2005)). A and K indicate the content of Al_2O_3 and K_2O respectively. CIA values are calculated and shown on the left side, with values correlated with on the CN-A-K ternary. Samples from the delta have the lowest CIA values and indicate high contents of CaO and Na_2O and plagioclase. Abbreviations: sm (smectite), pl (plagioclase), ksp (K-feldspar), il (illite), m (muscovite). B) Geochemical classification of sediments from the Indus delta (Clift et al., 2010), Indus Canyon (Li et al., 2018) and western Indian Peninsular shelf north of Goa (Kurian et al., 2013) following the scheme of Herron (1988). Phase 1 and Phase 2 sediments, together with the hemipelagic drape are the materials of the MTC.

Figure 14. Cross plot of Sr versus Nd isotope data from the MTC, adjacent drill sites, major source regions onshore, and modern Mahi, Tapti, and Narmada River sediments (Goswami et al., 2012). Kirthar and Sulaiman data is from Zhuang et al. (2015). Deccan Plateau data are from GEOROC compilation (http://georoc.mpch-mainz.gwdg.de/georoc/). Transhimalaya data are from Rolland et al. (2002), Singh et al. (2002), and Khan et al. (1997). Greater Himalayan data are from Ahmad et al.(2000), Deniel et al. (1987), Inger et al. (1993) and Parrish and Hodges (1996). Karakoram data are from Crawford and Searle (1992) and Schärer et al. (1990),

Figure 15. Downhole plots of Nd and Sr isotope compositions and clay mineralogy of siliciclastic sediments from IODP sites (A) U1456 and (B) U1457. Gray vertical bar shows compositional range of Quaternary sediments in the Indus Delta (Clift et al., 2010; Clift et al., 2008b), as well as modern Tapti and Narmada River sediments (Goswami et al., 2012). Deccan Plateau volcanic rocks plot outside this range at more positive ε_{Nd} values and lower $^{87}Sr/^{86}Sr$ values. Nd and Sr isotope analyses include errors recently suggested by Jonell et al. (2018) for bulk sediment compositions. Error bars encompass the total expected error for any bulk sample as a result of variable grain size and mineralogy, and analytical error contributed during sample preparation, homogenization, and analysis.

Figure 16. Kernel density estimate (KDE) plots for detrital zircon U-Pb ages for the Nataraja MTC compared to major source terrains in the western Himalayas, from the compilation of Alizai et al. (2011), as well as a modern sand from the river mouth (Clift et al., 2004) and select Indus Fan turbidites also from IODP Sites U1456 and U1457 (Clift et al., 2018). Deccan zircons

at ~65 Ma would plot within the Karakoram-Kohistan range but the inset box at the top shows that grains <100 Ma from the MTC do not cluster at this age and are better match to sources in the Indus suture zone. Data from the Tethyan, Greater and Lesser Himalaya are compiled from DeCelles et al. (2004). Karakoram data is from Le Fort et al. (1983), Parrish and Tirrul (1989), Schärer et al. (1990), Fraser et al. (2001) and Ravikant et al. (2009). Nanga Parbat data is from Zeitler and Chamberlain (1991) and Zeitler et al. (1993), Transhimalayan data is from Honegger et al. (1982), Schärer et al. (1984), Krol et al. (1996), Weinberg and Dunlap (2000), Zeilinger et al. (2001), Dunlap and Wysoczanski (2002), (Singh et al., 2007), and Ravikant et al. (2009).

Figure 17. Ternary diagram of clay minerals from IODP Site U1456 and U1457 indicates a clay mineral assemblage consisting mostly of smectite, chlorite and illite. Clay mineral data from source regions are plotted to compare their clay assemblages. Data from western Indian shelf modern sediments are from Rao and Rao (1995), Indus canyon data is from Li et al. (2018), Indus flood plain and delta data is from Alizai et al. (2012), and Indus Fan data is from Peng Zhou (unpublished).

Figure 18. (A) Interpretation of the depth-converted seismic section of the western Indian continental shelf immediately to the south of the source region for the Nataraja Slide based on the seismic profile of Nair and Pandey (2018) and using the seismic velocities shown in Table 5; and (B) A calculated sediment budget for the Indian shelf derived from two-dimensional sediment backstripping of this profile derived from FlexDecomp™ software.

Figure 19. Schematic cartoon illustrating the over-steepened Indian margin (A), the first phase of emplacement of the Nataraja MTC (B) separated by a short time of quiescence with hemipelagic sedimentation (C) from the second smaller phase of emplacement (D).

Table 1. Bulk sediment geochemistry analyzed by ICP-ES.

Table 2. Neodymium and strontium isotope data.

Table 3. Heavy mineral data. HM = heavy minerals; tHM = transparent heavy minerals. The ZTR index is the sum of zircon, tourmaline and rutile over total transparent heavy minerals (Hubert, 1962) and is classically used to estimate the mineralogical durability of the assemblage (i.e., the extent of recycling and/or intrastratal dissolution).

Table 4. U-Pb zircon data for sample U1456C-71R-1, 110 cm.

Table 5. Quantitative estimates of major clay mineral assemblages.

Table 6. Seismic interval velocities for the main stratigraphic units interpreted by Nair and Pandey (2018) used to depth convert the seismic profile before backstripping.

References

Ahmad, T., Harris, N., Bickle, M., Chapman, H., Bunbury, J., and Prince, C., 2000, Isotopic constraints on the structural relationships between the Lesser Himalayan Series and the High Himalayan Crystalline Series, Garhwal Himalaya: Geological Society of America Bulletin, v. 112, no. 3, p. 467-477.

Alizai, A., Carter, A., Clift, P. D., VanLaningham, S., Williams, J. C., and Kumar, R., 2011, Sediment provenance, reworking and transport processes in the Indus River by U-Pb dating of detrital zircon grains: Global and Planetary Change, v. 76, p. 33-55. doi:10.1016/j.gloplacha.2010.11.008.

Alizai, A., Hillier, S., Clift, P. D., and Giosan, L., 2012, Clay mineral variations in Holocene terrestrial sediments from the Indus Basin; a response to SW Asian Monsoon variability: Quaternary Research, v. 77, no. 3, p. 368–381. doi:10.1016/j.yqres.2012.01.008.

Andò, S., and Garzanti, E., 2014, Raman spectroscopy in heavy-mineral studies. In Sediment Provenance Studies, *in* Scott, R. A., Smyth, H. R., Morton, A. C., and Richardson, N., eds., Sediment Provenance Studies in Hydrocarbon Exploration and Production, Volume 386: London, Geological Society, p. 395–412.

Ando, S., Garzanti, E., Padoan, M., and Limonta, M., 2012, Corrosion of heavy minerals during weathering and diagenesis: a catalogue for optical analysis: Sedimentary Geology, v. 280, p. 165–178.

Bassi, D., and Nebelsick, J. H., 2000, Calcareous algae from the lower Oligocene Gornji Grad beds of Northern Slovenia: Rivista Italiana di Paleontologia e Stratigrafia, v. 106, p. 99-122.

Bea, R. G., Sircar, P., and Niedoroda, A. W., 1983, Wave-induced slides in South Pass Block 70, Mississippi Delta: Journal of Geotechnical Engineering, v. 109, p. 619–644.

Bhattacharya, G. C. B., Chaubey, A. K., Murty, G. P. S., Srinivas, S., Sarma, K. V., Subrahmanyam, V., and Krishna, K. S., 1994, Evidence for seafoor spreading in the Laxmi Basin, northeastern Indian Ocean: Earth and Planetary Science Letters, v. 125, p. 211-220.

Bilham, R., 1999, Slip parameters for the Rann of Kachchh, India, 16 June 1819, earthquake, quantified from contemporary accounts, *in* Stewart, I. S., and Vita-Finzi, C., eds., Coastal Tectonics, Volume 146: London, Geological Society, p. 295-319.

Bilham, R., Bendick, R., and Wallace, K., 2003, Flexure of the Indian Plate and intraplate earthquakes: Proceedings of the Indian Academy of Sciences (Earth and Planetary Sciences), v. 112,, p. 1–14.

Biswas, S. K., 2005, A review of structure and tectonics of Kutch basin, western India, with special reference to earthquakes: Current science, v. 88, no. 10, p. 1592-1600.

BouDagher-Fadel, M., 2018, Evolution and geological significance of larger benthic foraminifera, London, UCL Press, 702 p.

Bryn, P., Berg, K., Stoker, M. S., Haflidason, H., and Solheim, A., 2005, Contourites and their relevance for mass wasting along the Mid-Norwegian Margin.: Marine and Petroleum Geology, v. 22, p. 85-96.

Burg, J. P., Bernoulli, D., Smit, J., Dolati, A., and Bahroudi, A., 2008, A giant catastrophic mud-and-debris flow in the Miocene Makran: Terra Nova, v. 20, no. 3, p. 188-193.

Callot, P., Sempere, T., Odonne, F., and Robert, E., 2008, Giant submarine collapse of a carbonate platform at the Turonian-Coniacian transition: the Ayabacas formation, southern Peru: Basin Research, v. 20, p. 333–357.

Calvès, G., Huuse, M., Clift, P. D., and Brusset, S., 2015, Giant fossil mass wasting off the coast of West India: The Nataraja submarine slide: Earth and Planetary Science Letters, v. 432, p. 265–272. doi:10.1016/j.epsl.2015.10.022.

Carracedo, J. C., 1999, Growth, structure, instability and collapse of Canarian volcanoes and comparisons with Hawaiian volcanoes: Journal of Volcanology and Geothermal Research, v. 94, no. 1-4, p. 1-19.

Carter, A., and Bristow, C. S., 2003, Linking hinterland evolution and continental basin sedimentation by using detrital zircon thermochronology; a study of the Khorat Plateau basin, eastern Thailand: Basin Research, v. 15, p. 271–285.

Carter, R. M., 1975, A discussion and classification of subaqueous mass-transport with particular application to grain-flow, slurry-flow, and fluxoturbidites: Earth-Science Reviews, v. 11, no. 2, p. 145-177.

Chowdhary, L. R., 2004, Petroleum Geology of the Cambay Basin, Gujarat., India, Indian Petroleum Publishers, 171 p.

Clift, P., Gaedicke, C., Edwards, R., Lee, J., II, Hildebrand, P., Amjad, S., White, R. S., and Schlueter, H.-U., 2002, The stratigraphic evolution of the Indus Fan and the history of sedimentation in the Arabian Sea: Marine Geophysical Researches, v. 23, no. 3, p. 223-245.

Clift, P. D., 2006, Controls on the erosion of Cenozoic Asia and the flux of clastic sediment to the ocean: Earth and Planetary Science Letters, v. 241, no. 3-4, p. 571-580.

Clift, P. D., and Blusztajn, J. S., 2005, Reorganization of the western Himalayan river system after five million years ago: Nature, v. 438, no. 7070, p. 1001-1003.

Clift, P. D., Campbell, I. H., Pringle, M. S., Carter, A., Zhang, X., Hodges, K. V., Khan, A. A., and Allen, C. M., 2004, Thermochronology of the modern Indus River bedload; new insight into the control on the marine stratigraphic record: Tectonics, v. 23, no. TC5013. doi:10.1029/2003TC001559.

Clift, P. D., Giosan, L., Blusztajn, J., Campbell, I. H., Allen, C. M., Pringle, M., Tabrez, A., Danish, M., Rabbani, M. M., Carter, A., and Lückge, A., 2008a, Holocene erosion of the Lesser Himalaya triggered by intensified summer monsoon: Geology, v. 36, no. 1, p. 79–82. doi: 10.1130/G24315A.1.

Clift, P. D., Giosan, L., Carter, A., Garzanti, E., Galy, V., Tabrez, A. R., Pringle, M., Campbell, I. H., France-Lanord, C., Blusztajn, J., Allen, C., Alizai, A., Lückge, A., Danish, M., and Rabbani, M. M., 2010, Monsoon control over erosion patterns in the Western Himalaya: possible feed-backs into the tectonic evolution, *in* Clift, P. D., Tada, R., and Zheng, H., eds., Monsoon evolution and tectonic-climate linkage in Asia, Volume 342: London, Geological Society, p. 181–213.

Clift, P. D., Hodges, K., Heslop, D., Hannigan, R., Hoang, L. V., and Calves, G., 2008b, Greater Himalayan exhumation triggered by Early Miocene monsoon intensification: Nature Geoscience, v. 1, p. 875-880. doi:10.1038/ngeo351.

Clift, P. D., Shimizu, N., Layne, G., Gaedicke, C., Schlüter, H. U., Clark, M. K., and Amjad, S., 2001, Development of the Indus Fan and its significance for the erosional history of the western Himalaya and Karakoram: Geological Society of America Bulletin, v. 113, p. 1039–1051.

Clift, P. D., Zhou, P., Stockli, D. F., and Blusztajn, J., 2018, An Erosional Record of Regional Exhumation of the Western Himalaya and Karakoram: Nature Communications, v. in review.

Coleman, J., and Prior, D., 1988, Mass wasting on continental margins: Annual Review of Earth and Planetary Sciences, v. 16, no. 1, p. 101-119.

Crawford, M. B., and Searle, M. P., 1992, Field relationships and geochemistry of pre-collisional (India-Asia) granitoid magmatism in the central Karakoram, northern Pakistan: Tectonophysics, v. 206, no. 1-2, p. 171-192.

Dan, G., Sultan, N., and Savoye, B., 2007, The 1979 Nice harbour catastrophe revisited: trigger mechanism inferred from geotechnical measurements and numerical modelling: Marine Geology, v. 245, p. 40–64.

Davies, R., and Clark, I., 2006, Submarine slope failure primed and triggered by silica and its diagenesis: Basin Research, v. 18, p. 339-350.

DeCelles, P. G., Gehrels, G. E., Najman, Y., Martin, A. J., Carter, A., and Garzanti, E., 2004, Detrital geochronology and geochemistry of Cretaceous-Early Miocene strata of Nepal: implications for timing and diachroneity of initial Himalayan orogenesis: Earth and Planetary Science Letters, v. 227, no. 3-4, p. 313-330.

DeCelles, P. G., Gehrels, G. E., Quade, J., LaReau, B., and Spurlin, M., 2000, Tectonic implications of U-Pb zircon ages of the Himalayan orogenic belt in Nepal: Science, v. 288, no. 5465, p. 497-499. doi:10.1126/science.288.5465.497.

DeCelles, P. G., Kapp, P., Gehrels, G. E., and Ding, L., 2014, Paleocene-Eocene foreland basin evolution in the Himalaya of southern Tibet and Nepal: Implications for the age of initial India-Asia collision: Tectonics, v. 33, p. 824–849. doi:10.1002/ 2014TC003522.

Deniel, C., Vidal, P., Fernandez, A., Fort, P., and Peucat, J.-J., 1987, Isotopic study of the Manaslu granite (Himalaya, Nepal): inferences on the age and source of Himalayan leucogranites: Contributions to Mineralogy and Petrology, v. 96, no. 1, p. 78-92.

Derry, L. A., and France-Lanord, C., 1996, Neogene Himalayan weathering history and river $^{87}Sr/^{86}Sr$; impact on the marine Sr record: Earth and Planetary Science Letters, v. 142, p. 59-74.

Donelick, R. A., O'Sullivan, P. B., and Ketcham, R. A., 2005, Apatite fission-track analysis: Reviews in Mineralogy and Geochemistry, v. 58, no. 1, p. 49-94.

Dunham, R. J., 1962, Classification of carbonate rocks according to depositional texture, *in* Ham, W. E., ed., Classification of Carbonate Rocks, Volume 1, American Association of petroleum geology, p. 108–121.

Dunlap, W. J., and Wysoczanski, R., 2002, Thermal evidence for Early Cretaceous metamorphism in the Shyok suture zone and age of the Khardung volcanic rocks, Ladakh, India: Journal of Asian Earth Sciences, v. 20, no. 5, p. 481-490.

Ekdale, A. A., Bromley, R. G., and Pemberton, S. G., 1984, Ichnology. Trace fossils in sedimentation and stratigraphy, Tulsa, OK, Society of Economic Palaeontologists and Mineralogists, Short Course, 317 p.

Elverhoi, A., Breien, H., Blasio, F. V. D., Harbitz, C. B., and Pagliardi, M., 2010, Submarine landslides and the importance of the initial sediment composition for run-out length and final deposit: Ocean Dynamics, v. 60, p. 1027–1046. doi 10.1007/s10236-010-0317-z.

Embley, R. W., and Jacobi, R. D., 1977, Distribution and morphology of large submarine sediment slides and slumps on Atlantic continental margins: Marine Georesources & Geotechnology, v. 2, no. 1-4, p. 205-228.

Evans, D., McGiveron, S., Harrison, Z., Bryn, P., and Berg, K., 2002, Along-slope variation in the late Neogene evolution of the mid-Norwegian margin in response to uplift and tectonism, *in* Dore, A. G., Cartwright, J. A., Stoker, S., Turner, J. P., and White, N., eds., Exhumation of the North Atlantic Margin: Timing, Mechanisms and Implications for Petroleum Exploration, Volume 196: London, Geological Society, p. 139-151.

Farrell, S. G., 1984, A dislocation model applied to slump structures, Ainsa Basin, South Central Pyrenees: Journal of Structural Geology, v. 6, p. 727-736.

Fedo, C. M., Nesbitt, H. W., and Young, G. M., 1995, Unraveling the effects of potassium metasomatism in sedimentary rocks and paleosols, with implications for paleoweathering conditions and provenance: Geology, v. 23, p. 921–924.

Fraser, J. E., Searle, M. P., Parrish, R. R., and Noble, S. R., 2001, Chronology of deformation, metamorphism, and magmatism in the southern Karakoram Mountains: Geological Society of America Bulletin, v. 113, no. 11, p. 1443-1455.

Frey Martinez, J., Cartwright, J., and Hall, B., 2005, 3D seismic interpretation of slump complexes: examples from the continental margin of Israel: Basin Research, v. 17, p. 83-108.

Gamboa, D., Alves, T., and Cartwright, J., 2012, Seismic-Scale Rafted and Remnant Blocks over Salt Ridges in the Espírito Santo Basin, Brazil, *in* Yamada, Y., Kawamura, K., Ken Ikehara, Ogawa, Y., Urgeles, R., Mosher, D., Chaytor, J., and Strasser, M., eds., Submarine Mass Movements and Their Consequences: Dordrecht, Springer, p. 629-638.

Garzanti, E., 2017, The maturity myth in sedimentology and provenance analysis: Journal of Sedimentary Research, v. 87, p. 353-365.

Garzanti, E., and Andò, S., 2007, Heavy-mineral concentration in modern sands: implications for provenance interpretation, *in* Mange, M., and Wright, D., eds., Heavy Minerals in Use, Volume 58: Amsterdam, Elsevier, p. 517-545.

Garzanti, E., Andò, S., and Vezzoli, G., 2009, Grain-size dependence of sediment composition and environmental bias in provenance studies: Earth and Planetary Science Letters, v. 277, no. 3-4, p. 422-432.

Garzanti, E., Vezzoli, G., Ando, S., Paparella, P., and Clift, P. D., 2005, Petrology of Indus River sands; a key to interpret erosion history of the western Himalayan syntaxis: Earth and Planetary Science Letters, v. 229, no. 3-4, p. 287-302. DOI: 10.1016/j.epsl.2004.11.008.

Gehrels, G. E., Kapp, P., DeCelles, P., Pullen, A., Blakely, R., Weislgel, A., Ding, L., Guynn, J., Marin, A., McQuarrie, N., and Yin, A., 2011, Detrital zircon geochronology of pre-Tertiary strata in the Tibetan-Himalayan orogen: Tectonics, v. 30, no. TC5016. doi:10.1029/2011TC002868.

Goldstein, S. L., O'Nions, R. K., and Hamilton, P. J., 1984, A Sm-Nd isotopic study of atmospheric dusts and particulates from major river systems: Earth and Planetary Science Letters, v. 70, no. 2, p. 221-236.

Goswami, V., Singh, S. K., Bhushan, R., and Rai, V. K., 2012, Temporal variations in 87Sr/86Sr and eNd in sediments of the southeastern Arabian Sea: Impact of monsoon and surface water circulation: Geochemistry Geophysics Geosystems, v. 13, no. Q01001. doi:10.1029/2011GC003802.

Gradstein, F. M., Ogg, G., and Schmitz, M., 2012, The Geologic Time Scale 2012, New York, Elsevier.

Hampton, M. A., Lee, H. J., and Locat, J., 1996, Submarine landslides: Reviews of Geophysics, v. 34, no. 1, p. 33-59. doI:10.1029/95RG03287

Herron, M. M., 1988, Geochemical classification of terrigenous sands and shales from core or log data: Journal of Sedimentary Petrology, v. 58, p. 820–829.

Hine, A. C., 1992, Megabreccia shedding from modern, low-relief carbonate platforms, Nicaraguan Rise: Geological Society of America Bulletin, v. 104, p. 928–943.

Hodges, K., 2003, Geochronology and thermochronology in orogenic systems, *in* Rudnick, R., ed., The Crust: Amsterdam, Elsevier-Science, p. 263-292.

Honegger, K., Dietrich, V., Frank, W., Gansser, A., Thoni, M., and Trommsdorf, V. F., 1982, Magmatism and metamorphism in the Ladakh Himalayas (The Indus-Tsangpo suture zone): Earth and Planetary Science Letters, v. 60, p. 178-194.

Hsu, S.-K., Kuo, J., Lo, C.-L., Tsai, C.-H., Doo, W.-B., Ku, C.-Y., and Sibuet, J.-C., 2008, Turbidity currents, submarine landslides and the 2006 Pingtung earthquake off SW Taiwan: Terrestrial Atmospheric and Ocean Sciences, v. 19, no. 6, p. 767–772. . doi:10.3319/TAO.2008.19.6.767(PT).

Hubert, J. F., 1962, A zircon–tourmaline–rutile maturity index and the interdependence of the composition of heavy mineral assemblages with the gross composition and texture of sandstones: Journal of Sedimentary Petrology, v. 32, p. 440-450.

Inger, S., and Harris, N., 1993, Geochemical constraints on leucogranite magmatism in the Langtang Valley, Nepal Himalaya: Journal of Petrology, v. 34, no. 2, p. 345-368.

Kastens, K. A., 1984, Earthquakes as a triggering mechanism for debris flows and turbidites on the Calabrian Ridge: Marine Geology, v. 55, no. 1-2, p. 13-33.

Khan, M. A., Stern, R. J., Gribble, R. F., and Windley, B. F., 1997, Geochemical and isotopic constraints on subduction polarity, magma sources, and palaeogeography of the Kohistan intra-oceanic arc, northern Pakistan Himalaya: Journal of the Geological Society, London, v. 154, p. 935–946.

Khonde, N., Singh, S. K., Maurya, D. M., Rai, V. K., Chamyal, L. S., and Giosan, L., 2017, Tracing the Vedic Saraswati River in the Great Rann of Kachchh: Scientific Reports, v. 7, no. 5476. doi:10.1038/s41598-017-05745-8.

Klaus, A., Norris, R. D., Kroon, D., and Smit, J., 2000, Impact-induced mass wasting at the KT boundary: Blake Nose, western North Atlantic: Geology, v. 28, no. 4, p. 319-322.

Krastel, S., Wynn, R. B., Georgiopoulou, A., Geersen, J., Henrich, R. d., Meyer, M., and Schwenk, T., 2012, Large-Scale Mass Wasting on the Northwest African Continental Margin: Some General Implications for Mass Wasting on Passive Continental Margins, *in* Yamada, Y., Kawamura, K., Ken Ikehara, Ogawa, Y., Urgeles, R., Mosher, D., Chaytor, J., and Strasser, M., eds., Submarine Mass Movements and Their Consequences: Dordrecht, Springer, p. 189-200.

Krol, M. A., Zeitler, P. K., and Copeland, P., 1996, Episodic unroofing of the Kohistan Batholith, Pakistan: Implications from K-feldspar thermochronology: Journal of Geophysical Research-Solid Earth, v. 101, no. B12, p. 28149-28164.

Kurian, S., Nath, B. N., Kumar, N. C., and Nair, K. K. C., 2013, Geochemical and Isotopic Signatures of Surficial Sediments from the Western Continental Shelf of India: Inferring Provenance, Weathering, and the Nature of Organic Matter Geochemical and Isotopic Signatures of Sediments From The Indian West Coast: Journal of Sedimentary Research, v. 83, no. 6, p. 427-442. doi:10.2110/jsr.2013.36.

Kusznir, N. J., Roberts, A. M., and Morley, C. K., 1995, Forward and reverse modelling of rift basin formation, *in* Lambiase, J. J., ed., Hydrocarbon Habitat in Rift Basins, Volume 80: London, Geological Society, p. 33–56.

Lastras, G., Canals, M., Urgeles, R., De Batist, M., Calafat, A. M., and Casamor, J. L., 2004, Characterisation of the recent BIG'95 debris flow on the Ebro margin, Western Mediterranean Sea, after a variety of seismic reflection data: Marine Geology, v. 213, p. 235-255. doi:10.1016/j.margeo.2004.10.008.

Le Fort, P., Debon, F., and Sonet, J., 1983, Petrography, geochemistry and geochronology of some samples from the Karakoram Batholith (N. Pakistan), *in* Shams, F. A., ed., Granites of the Himalayas, Karakoram and Hindu Kush: Lahore, Pakistan, Punjab University, p. 377–387.

Leynaud, D., Mienert, J., and Vanneste, M., 2009, Submarine mass movements on glaciated and non-glaciated European continental margins: A review of triggering mechanisms and preconditions to failure: Marine and Petroleum Geology, v. 26, no. 5, p. 618-632.

Li, Y., 2018, Signal propagation, provenance, and climate records in the Indus Submarine Canyon since the Last Deglacial [PhD PhD]: Louisiana State University.

Li, Y., Clift, P. D., Böning, P., Blusztajn, J., Murray, R. W., Ireland, T., Pahnke, K., and Giosan, L., 2018, Continuous Signal Propagation in the Indus Submarine Canyon since the Last Deglacial: Marine Geology, v. 406, p. 159–176. doi:10.1016/j.margeo.2018.09.011.

Lowe, D. R., 1976, Grain flow and grain flow deposits: Journal of Sedimentary Research, v. 46, no. 1.

Lucente, C. C., and Pini, G. A., 2003, Anatomy and emplacement mechanism of a large submarine slide within a Miocene foredeep in the northern Apennines, Italy: a field perspective: American Journal of Science, v. 303, p. 565-602.

Mange, M. A., and Maurer, H. F. W., 1992, Heavy minerals in colour, London, Chapman and Hall, 147 p.

Martinsen, O. J., and Bakken, B., 1990, Extensional and compressional zones in slumps and slides in the Namurian of County Clare, Ireland: Journal of the Geological Society of London, v. 147, p. 153-164.

Mienert, J., Vanneste, M., Bünz, S., Andreassen, K., Haflidason, H., and Sejrup, H. P., 2005, Ocean warming and gas hydrate stability on the mid-Norwegian margin at the Storegga Slide: Marine and Petroleum Geology, v. 22, no. 1-2, p. 233-244.

Miles, P. R., and Roest, W. R., 1993, Earliest seafoor spreading magnetic anomalies in the north Arabian Sea and the ocean-continent transition: Geophysical Journal International, v. 115, p. 1025-1031.

Moernaut, J., De Batist, M., Charlet, F., Heirman, K., Chapron, E., Pino, M., Brümmer, R., and Urrutia, R., 2007, Giant earthquakes in South-Central Chile revealed by Holocene mass-wasting events in Lake Puyehue: Sedimentary Geology, v. 195, no. 3-4, p. 239-256.

Moore, D. G., 1961, Submarine slumps: Journal of Sedimentary Research, v. 31, no. 3, p. 343-357.

Mullins, H. T., Gardulski, A. F., and Hine, A. C., 1986, Catastrophic collapse of the west Florida carbonate platform margin: Geology v. 14, p. 167–170.

Nair, N., and Pandey, D. K., 2018, Cenozoic sedimentation in the Mumbai Offshore Basin: Implications for tectonic evolution of the western continental margin of India: Journal of Asian Earth Sciences, v. 152, p. 132-144. doi:10.1016/j.jseaes.2017.11.037.

Najman, Y., Appel, E., Boudagher-Fadel, M., Bown, P., Carter, A., Garzanti, E., Godin, L., Han, J., Liebke, U., Oliver, G., Parrish, R., and Vezzoli, G., 2010, Timing of India-Asia collision: Geological, biostratigraphic, and palaeomagnetic constraints: Journal of Geophysical Research, v. 115, no. B12416. doi:10.1029/2010JB007673.

Nesbitt, H. W., Markovics, G., and Price, R. C., 1980, Chemical processes affecting alkalis and alkaline earths during continental weathering: Geochimica et Cosmochimica Acta, v. 44, p. 1659–1666.

Pandey, D. K., Clift, P. D., Kulhanek, D. K., Andò, S., Bendle, J. A. P., Bratenkov, S., Griffith, E. M., Gurumurthy, G. P., Hahn, A., Iwai, M., Khim, B.-K., Kumar, A., Kumar, A. G., Liddy, H. M., Lu, H., Lyle, M. W., Mishra, R., Radhakrishna, T., Routledge, C. M., Saraswat, R., Saxena, R., Scardia, G., Sharma, G. K., Singh, A. D., Steinke, S., Suzuki, K., Tauxe, L., Tiwari, M., Xu, Z., and Yu, Z., 2016a, Site U1456, *in* Pandey, D. K., Clift, P. D., and Kulhanek, D. K., eds., Arabian Sea Monsoon. Proceedings of the International Ocean Discovery Program, Volume 355: College Station, TX, International Ocean Discovery Program.

-, 2016b, Site U1457, *in* Pandey, D. K., Clift, P. D., and Kulhanek, D. K., eds., Arabian Sea Monsoon. Proceedings of the International Ocean Discovery Program, Volume 355: College Station, TX, International Ocean Discovery Program.

Pandey, D. K., Clift, P. D., Kulhanek, D. K., and Expedition 355 Scientists, 2016c, Arabian Sea Monsoon: Proceedings of the International Ocean Discovery Program, v. 355. doi:10.14379/iodp.proc.355.2016.

Pandey, O. P., Agrawal, P. K., and Negi, J. G., 1995, Lithospheric structure beneath Laxmi Ridge and late Cretaceous geodynamic events: Geo-Marine Letters, v. 15, p. 85-91.

Parnell, J., 2008, Global mass wasting at continental margins during Ordovician high meteorite influx: Nature Geoscience, v. 2, p. 57. doi:10.1038/ngeo386.

Parrish, R. R., and Hodges, K. V., 1996, Isotopic constraints on the age and provenance of the Lesser and Greater Himalayan sequences, Nepalese Himalaya: Geological Society of America Bulletin, v. 108, no. 7, p. 904-911.

Parrish, R. R., and Tirrul, R., 1989, U-Pb age of the Baltoro Granite, Northwest Himalaya, and implications for monazite U-Pb systematics: Geology, v. 17, p. 1076–1079.

Peters, S. E., and Loss, D. P., 2012, Storm and fair-weather wave base: A relevant distinction?: Geology, v. 40, no. 6, p. 511-514.

Pickering, K., Stow, D., Watson, M., and Hiscott, R., 1986, Deep-water facies, processes and models: a review and classification scheme for modern and ancient sediments: Earth-Science Reviews, v. 23, no. 2, p. 75-174.

Piper, D. J., Shor, A. N., Farre, J. A., O'Connell, S., and Jacobi, R., 1985, Sediment slides and turbidity currents on the Laurentian Fan: Sidescan sonar investigations near the epicenter of the 1929 Grand Banks earthquake: Geology, v. 13, no. 8, p. 538-541.

Principaud, M., Mulder, T., Gillet, H., and Borgomano, J., 2015, Large-scale carbonate submarine mass-wasting along the northwestern slope of the Great Bahama Bank (Bahamas): Morphology, architecture, and mechanisms: Sedimentary Geology, v. 317, p. 27-42. doi:10.1016/j.sedgeo.2014.10.008.

Rao, R. P., and Talukdar, S. N., 1980, Petroleum geology of Bombay High field, India, *in* Halbouty, M. T., ed., Giant oil and gas fields of the decade: 1968–1978, Volume 30, American Association of Petroleum Geologists, p. 487–506.

Rao, V. P., and Rao, B. R., 1995, Provenance and distribution of clay minerals in the sediments of the western continental shelf and slope of India: Continental Shelf Research, v. 15, no. 14, p. 1757-1771. doi:10.1016/0278-4343(94)00092-2.

Ravikant, V., Wu, F. Y., and Ji, W. Q., 2009, Zircon U-Pb and Hf isotopic constraints on petrogenesis of the Cretaceous-Tertiary granites in eastern Karakoram and Ladakh, India: Lithos, v. 110, p. 153-166.

Rolland, Y., Picard, C., Pecher, A., Lapierre, H., Bosch, D., and Keller, F., 2002, The Cretaceous Ladakh arc of NW himalaya—slab melting and melt–mantle interaction during fast northward drift of Indian Plate: Chemical Geology, v. 182, p. 139–178.

Schärer, U., Copeland, P., Harrison, T. M., and Searle, M. P., 1990, Age, cooling history, and origin of post-collisional leucogranites in the Karakoram Batholith; a multi-system isotope study: The Journal of Geology, v. 98, no. 2, p. 233-251.

Schärer, U., Xu, R.-H., and Allègre, C. J., 1984, U-Pb geochronology of Gangdese (Transhimalaya) plutonism in the Lhasa-Xigaze region, Tibet: Earth and Planetary Science Letters, v. 69, no. 2, p. 311-320.

Schlager, W., Reijmer, J. J. G., and Droxler, A., 1994, Highstand shedding of carbonate platforms: Journal of Sedimentary Research, v. 64, no. 3b, p. 270-281. doi:10.1306/D4267FAA-2B26-11D7-8648000102C1865D.

Sclater, J. G., and Christie, P. A. F., 1980, Continental stretching: an explanation of the post Mid-Cretaceous subsidence of the central North Sea basin: Journal of Geophysical Research, v. 85, p. 3711–3739.

Seilacher, A., 1967, Bathymetry of trace fossils: Marine Geology, v. 5, p. 413–428.

Singh, M., Sharma, M., and Tobschall, H. J., 2005, Weathering of the Ganga alluvial plain, northern India: implications from fluvial geochemistry of the Gomati River: Applied Geochemistry, v. 20, p. 1-21.

Singh, S., Kumar, R., Barley, M. E., and Jain, A. K., 2007, SHRIMP U–Pb ages and depth of emplacement of Ladakh batholith, eastern Ladakh, India: Journal of Asian Earth Sciences, v. 30, no. 3, p. 490–503.

Singh, S. K., and France-Lanord, C., 2002, Tracing the distribution of erosion in the Brahmaputra watershed from isotopic compositions of stream sediments: Earth and Planetary Science Letters, v. 202, no. 3-4, p. 645-662.

Strachan, L. J., 2002, Slump-initiated and controlled syndepositional sandstone remobilisation: an example from the Namurian of County Clare, Ireland: Sedimentology, v. 49, p. 25-41.

Talling, P. J., Masson, D. G., Sumner, E. J., and Malgesini, G., 2012, Subaqueous sediment density flows: Depositional processes and deposit types: Sedimentology, v. 59, no. 7, p. 1937-2003.

Tappin, D. R., Watts, P., McMurtry, G. M., Lafoy, Y., and Matsumoto, T., 2001, The Sissano, Papua New Guinea tsunami of July 1998 – offshore evidence on the source mechanism: Marine Geology, v. 17, p. 1–23.

Trincardi, F., and Argnani, A., 1990, Gela Submarine slide: a major basin-wide event in the Plio-Quatemary foredeep of Sicily: Geo-marine Letters, v. 10, p. 13-21.

Vardy, M. E., Pinson, L. J., Bull, J. M., Dix, J. K., Henstock, T. J., Davis, J. W., and Gutowski, M., 2010, 3D seismic imaging of buried Younger Dryas mass movement flows: Lake Windermere, UK: Geomorphology, v. 118, no. 1-2, p. 176-187.

Vermeesch, P., 2004, How many grains are needed for a provenance study?: Earth and Planetary Science Letters, v. 224, p. 351–441.

Wandrey, C. J., 2004, Bombay Geologic Province Eocene to Miocene Composite Total Petroleum System, India: US Geological Survey, Department of the Interior, 2208-F.

Weinberg, R. F., and Dunlap, W. J., 2000, Growth and Deformation of the Ladakh Batholith, Northwest Himalayas: Implications for Timing of Continental Collision and Origin of Calc-Alkaline Batholiths: Journal of Geology, v. 108, p. 303–320. DOI: 10.1086/314405.

Yamada, Y., Kawamura, K., Ikehara, K., Ogawa, Y., Urgeles, R., Mosher, D., Chaytor, J., and Strasser, M., 2012, Submarine mass movements and their consequences, *in* Lykousis, V., Sakellariou, D., and Locat, J., eds., Submarine mass movements and their consequences, Springer, p. 1-12.

Zeilinger, G., Burg, J. P., Schaltegger, U., and Seward, D., 2001, New U/ Pb and fission track ages and their implication for the tectonic history of the lower Kohistan Arc Complex, northern Pakistan: Journal of Asian Earth Sciences, v. 19, no. 3S, p. 79-81.

Zeitler, P. K., and Chamberlain, C. P., 1991, Petrogenetic and Tectonic Significance of Young Leukogranites from the Northwestern Himalaya, Pakistan: Tectonics, v. 10, no. 4, p. 729-741.

Zeitler, P. K., Chamberlain, C. P., and Smith, H. A., 1993, Synchronous Anatexis, Metamorphism, and Rapid Denudation at Nanga-Parbat (Pakistan Himalaya): Geology, v. 21, no. 4, p. 347-350.

Zhuang, G., Najman, Y., Guillot, S., Roddaz, M., Antoine, P.-O., Métaise, G., Carter, A., Marivaux, L., and Solangig, S. H., 2015, Constraints on the collision and the pre-collision tectonic configuration between India and Asia from detrital geochronology, thermochronology, and geochemistry studies in the lower Indus basin, Pakistan: Earth and Planetary Science Letters, v. 432, p. 363–373. doi:10.1016/j.epsl.2015.10.026.

Figure 1

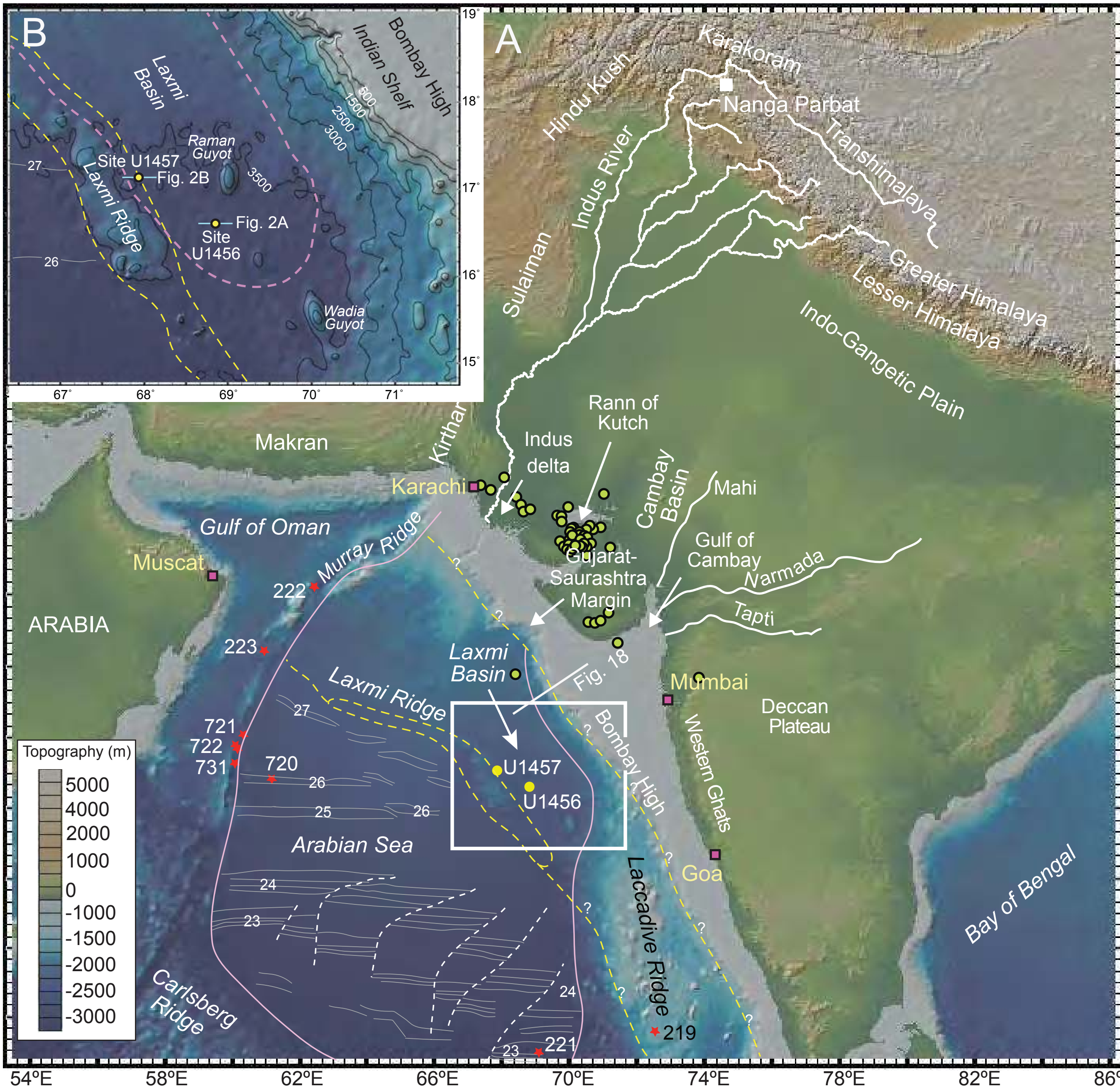

Figure 1
Dailey et al.

Figure 2

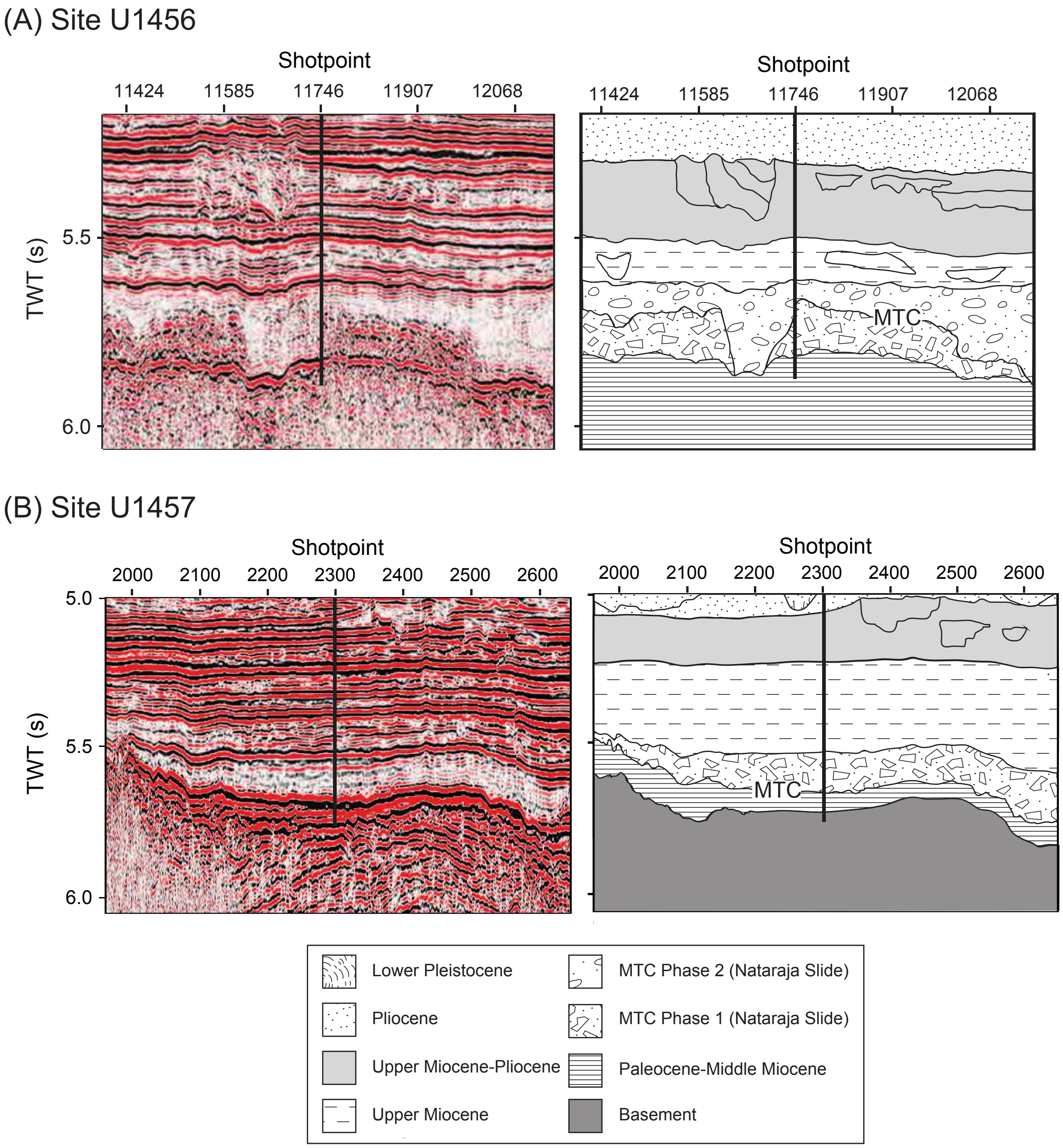

Figure 2
Dailey et al.

Figure 3

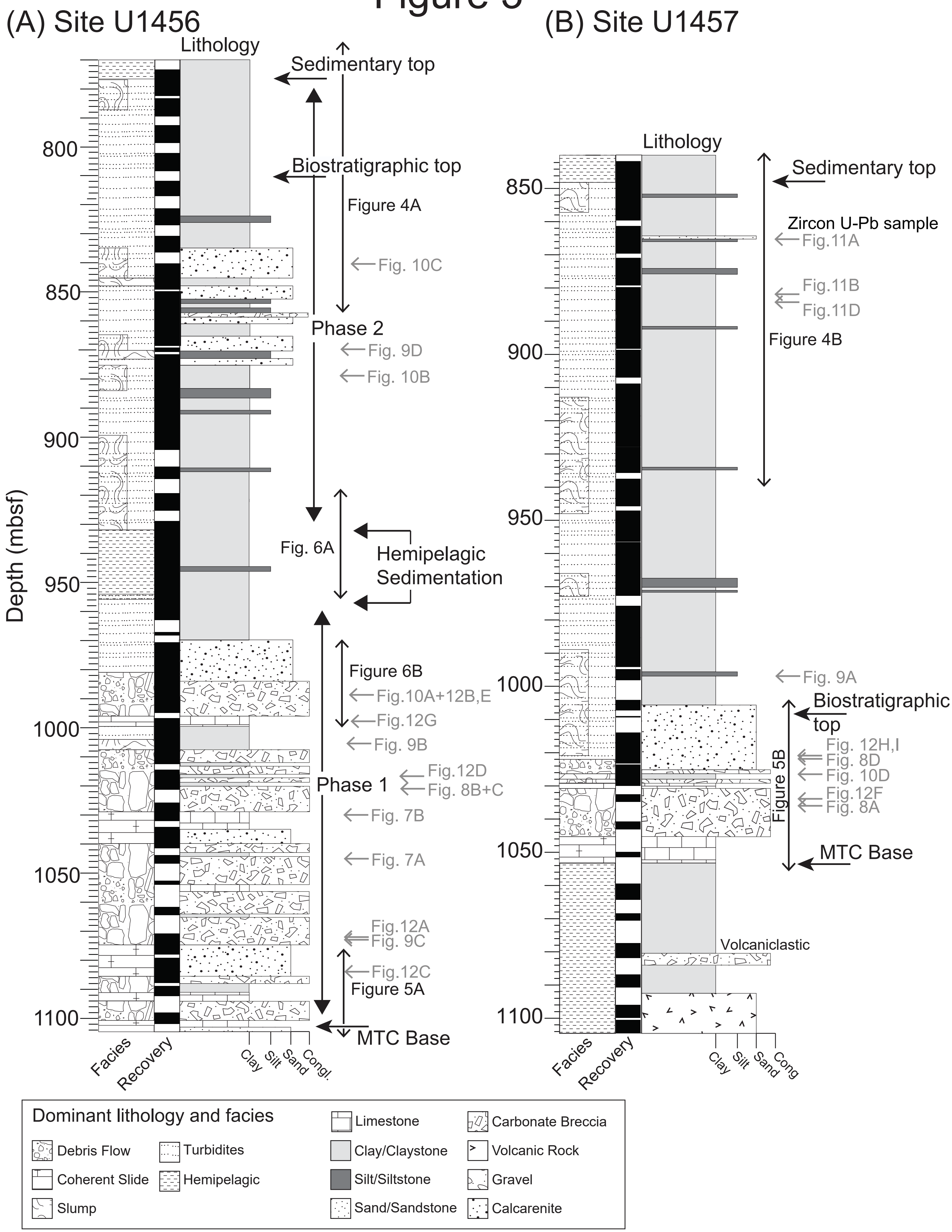

Figure 3
Dailey et al.

Figure 4

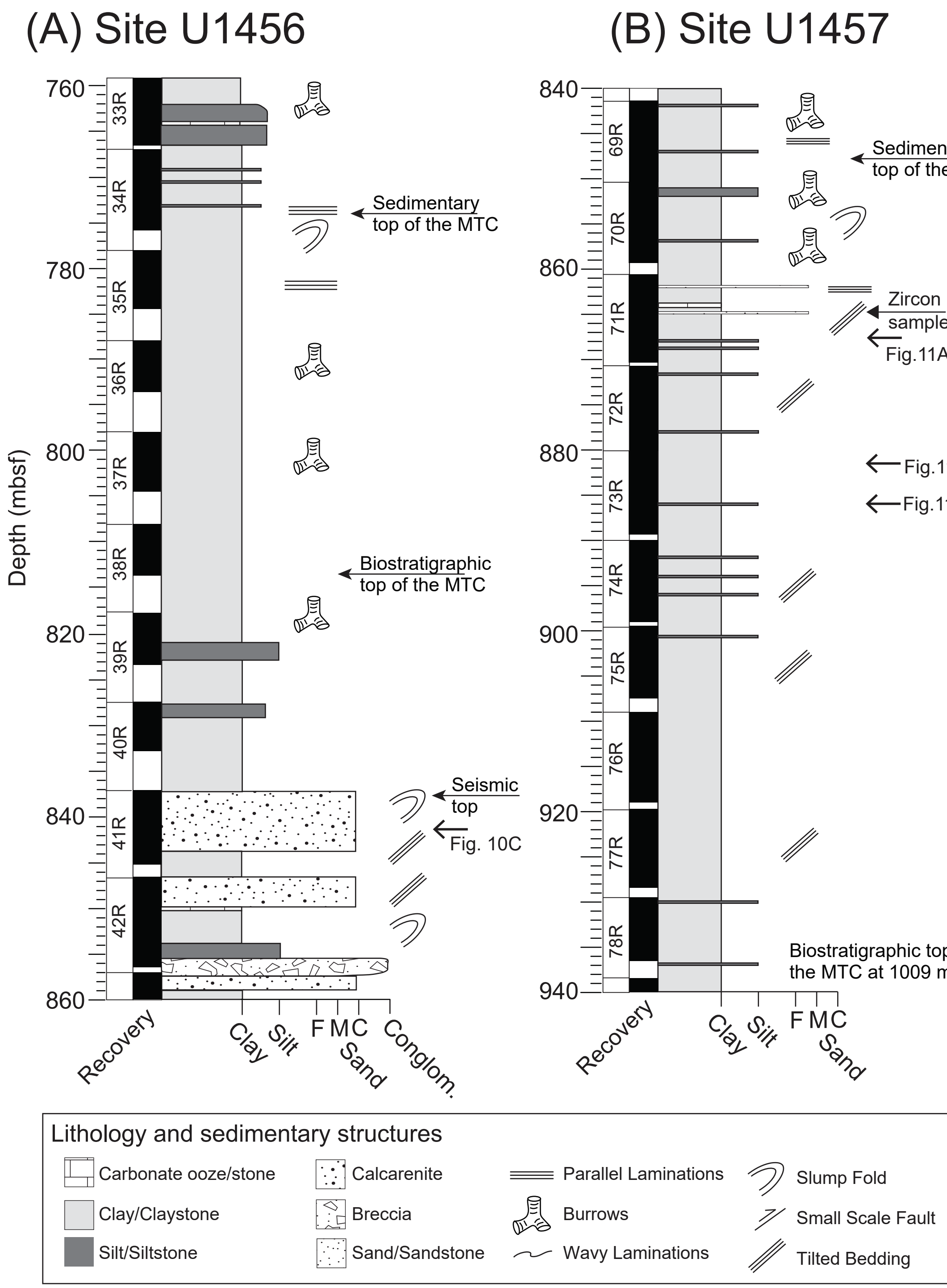

Figure 4
Dailey et al.

Figure 5

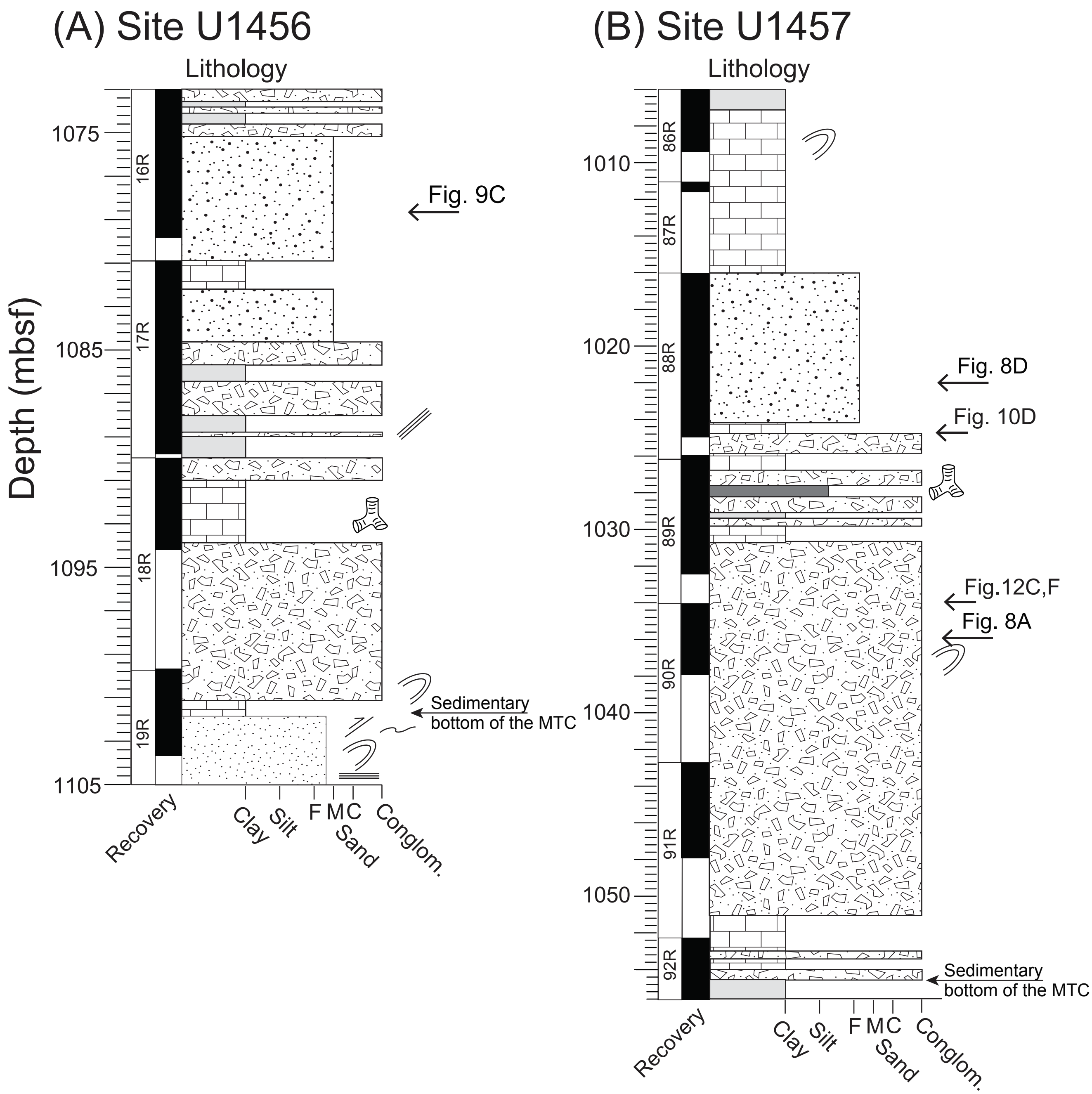

Figure 5
Dailey et al.

Figure 6

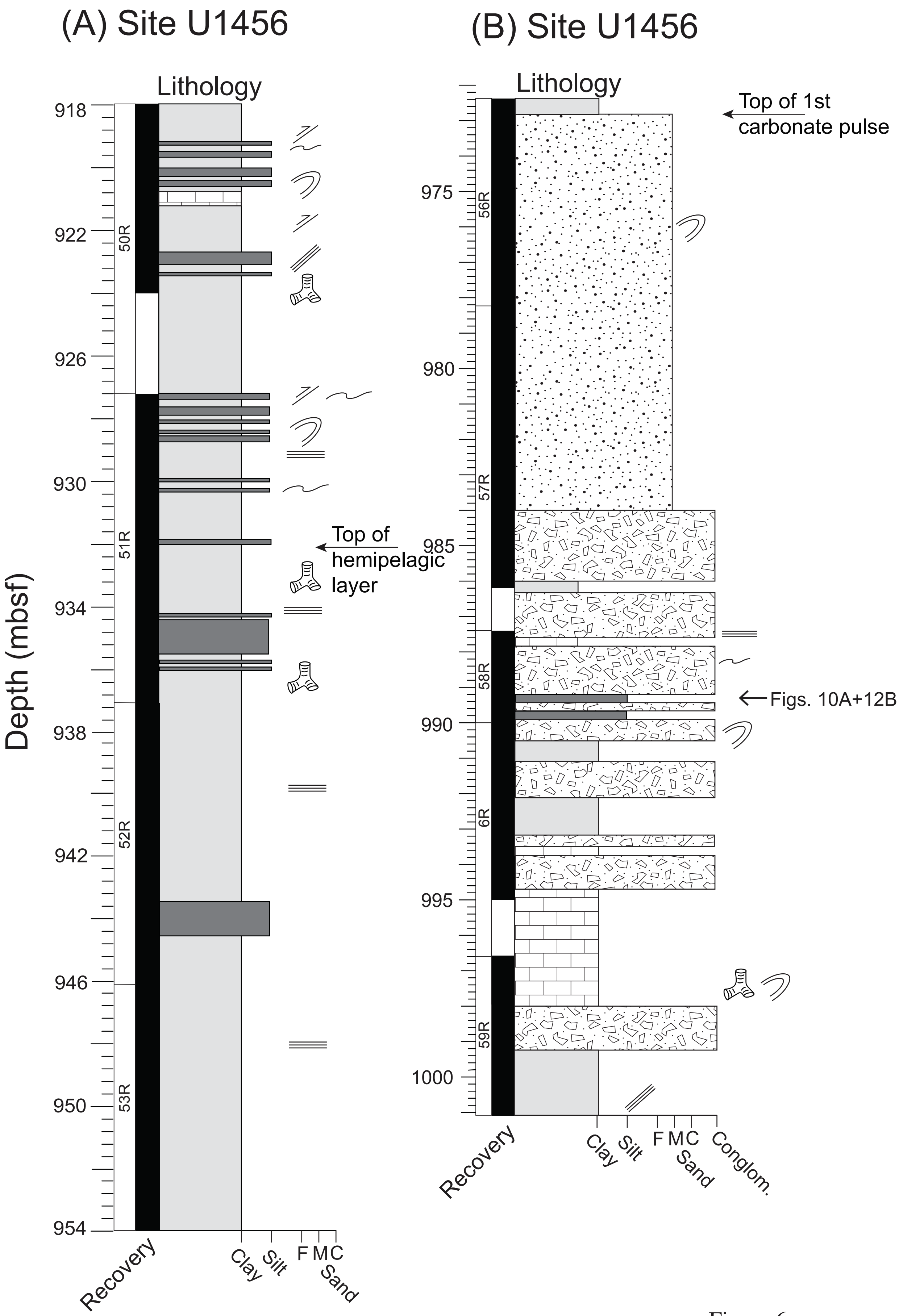

Figure 6
Dailey et al.

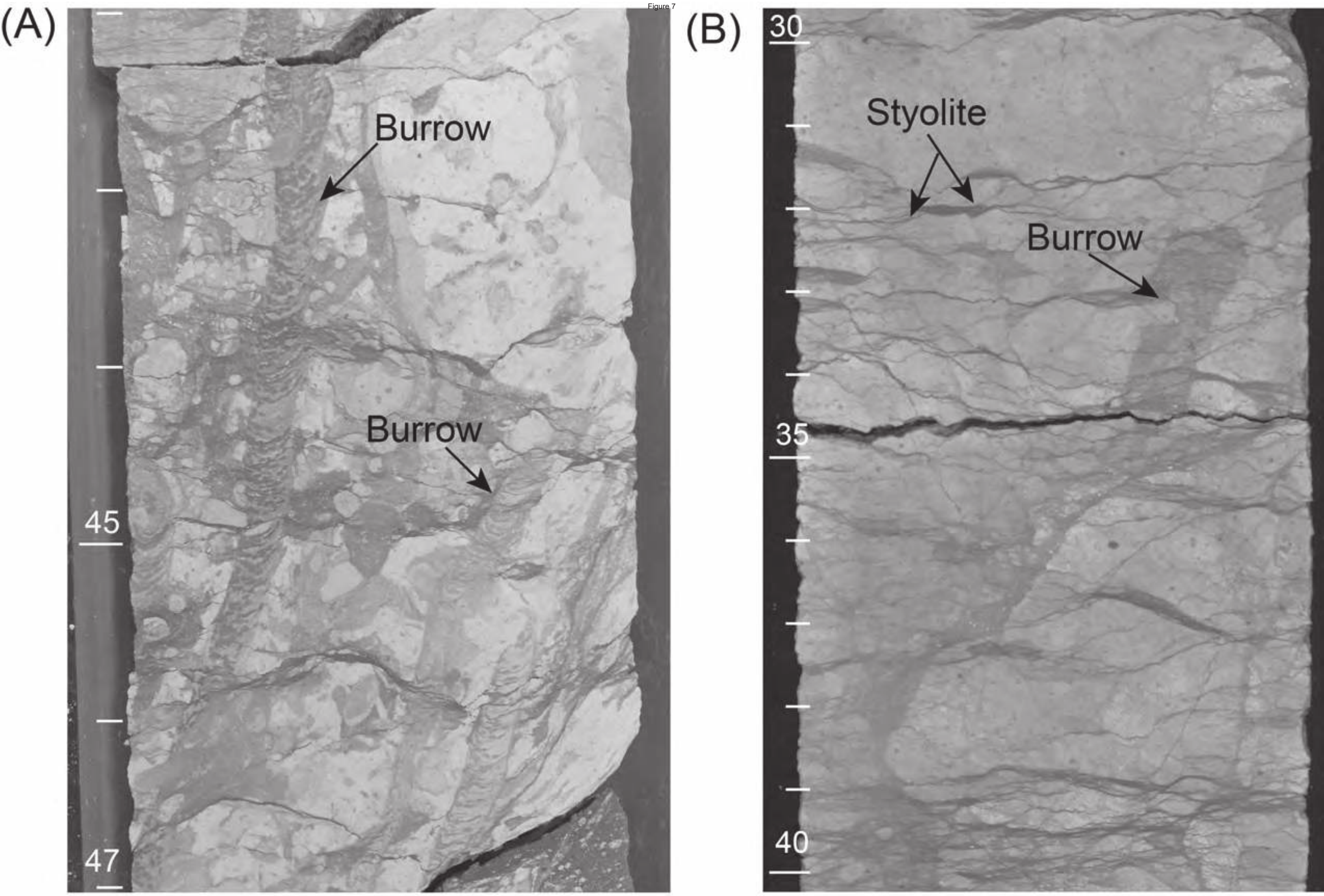

Figure 7
Dailey et al.

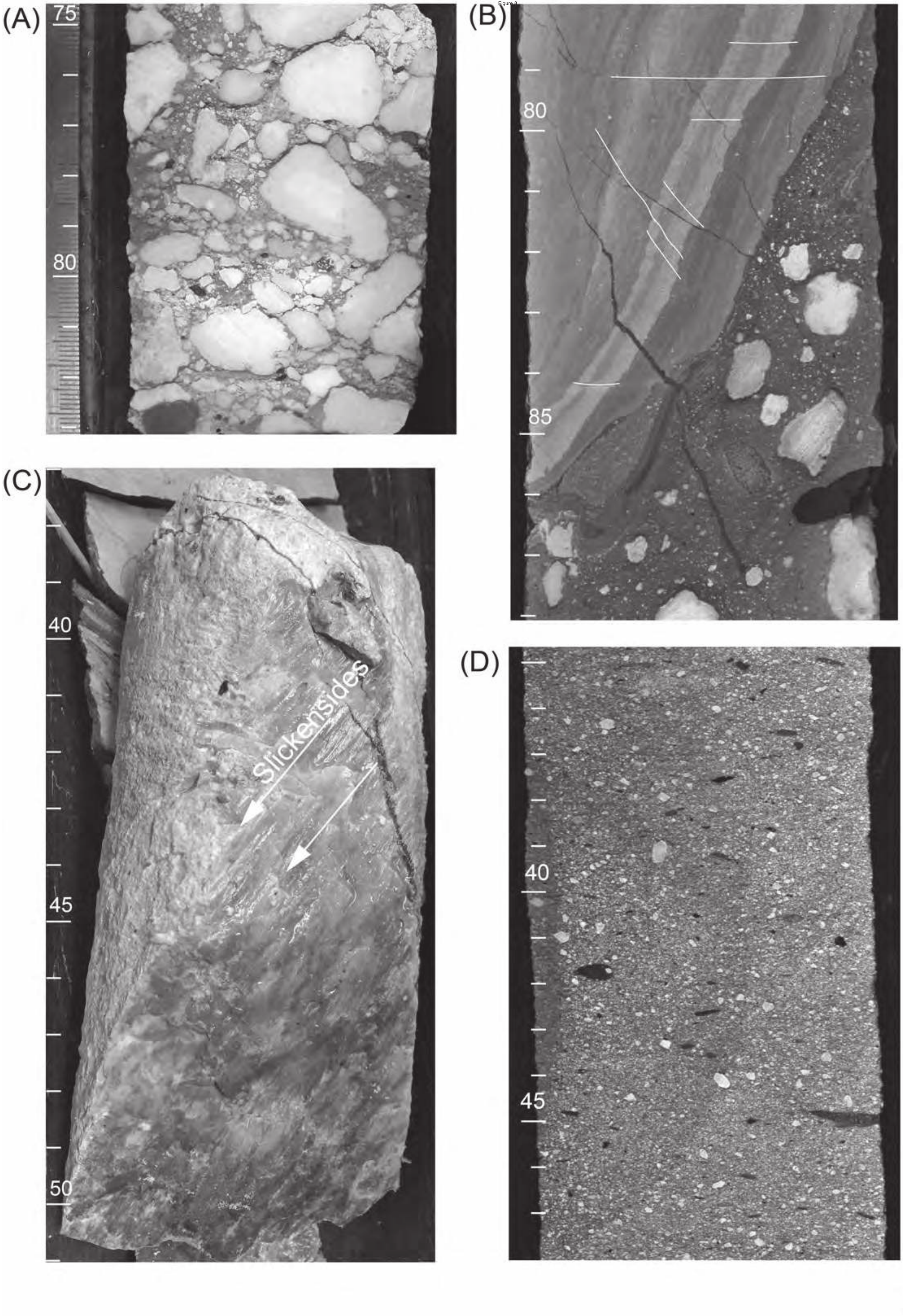

Figure 8
Dailey et al.

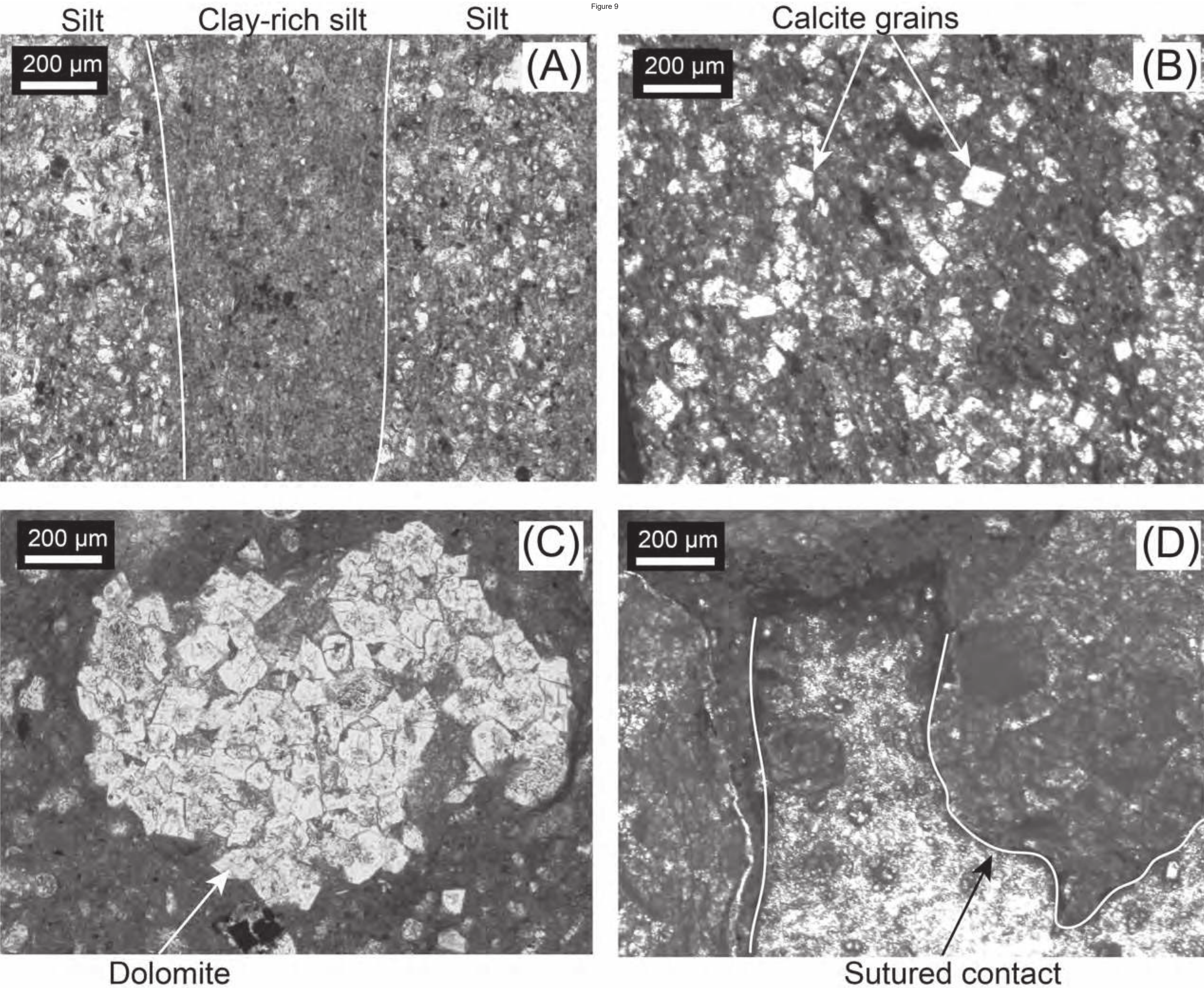

Figure 9
Dailey et al.

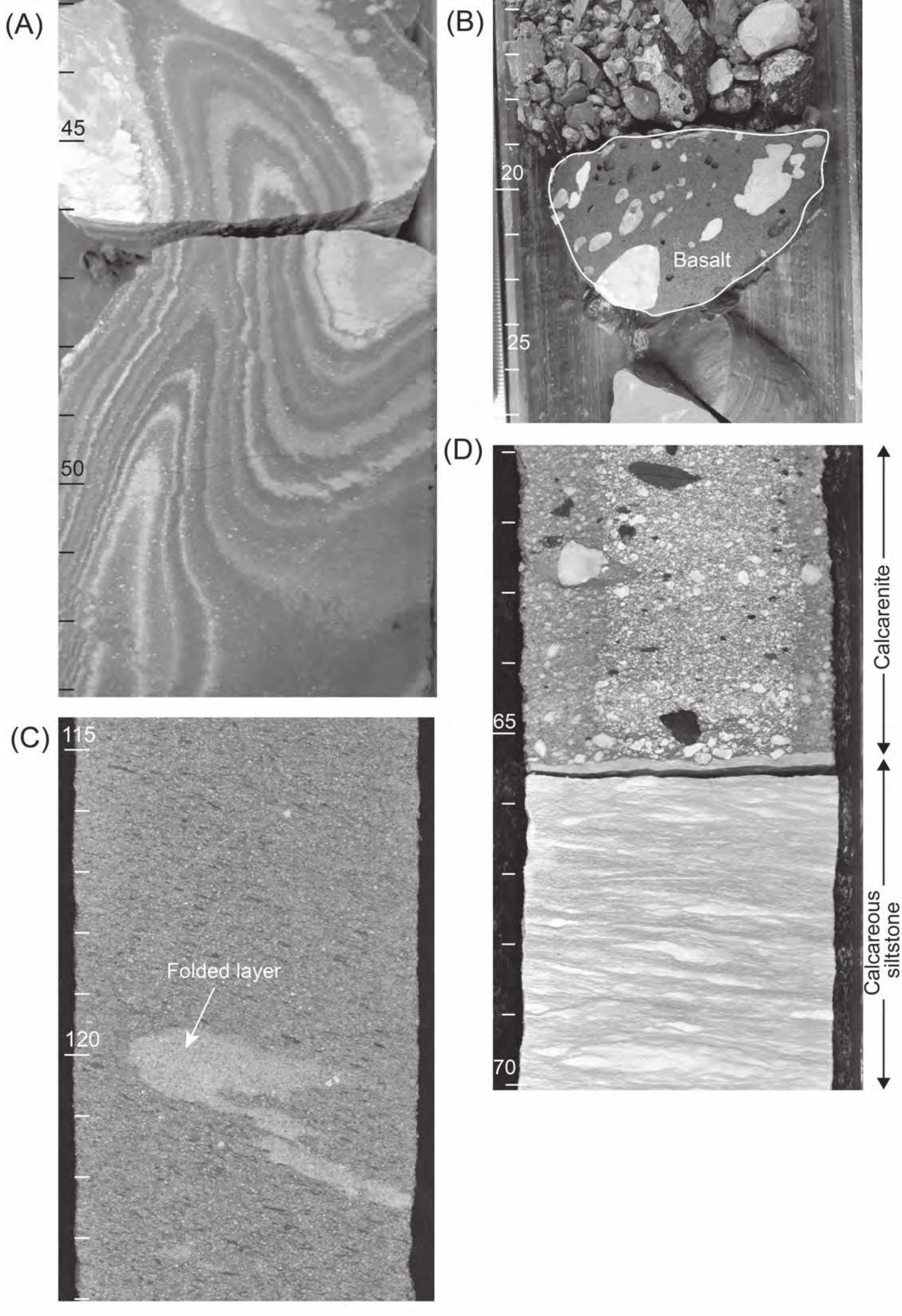

Figure 10
Dailey et al.

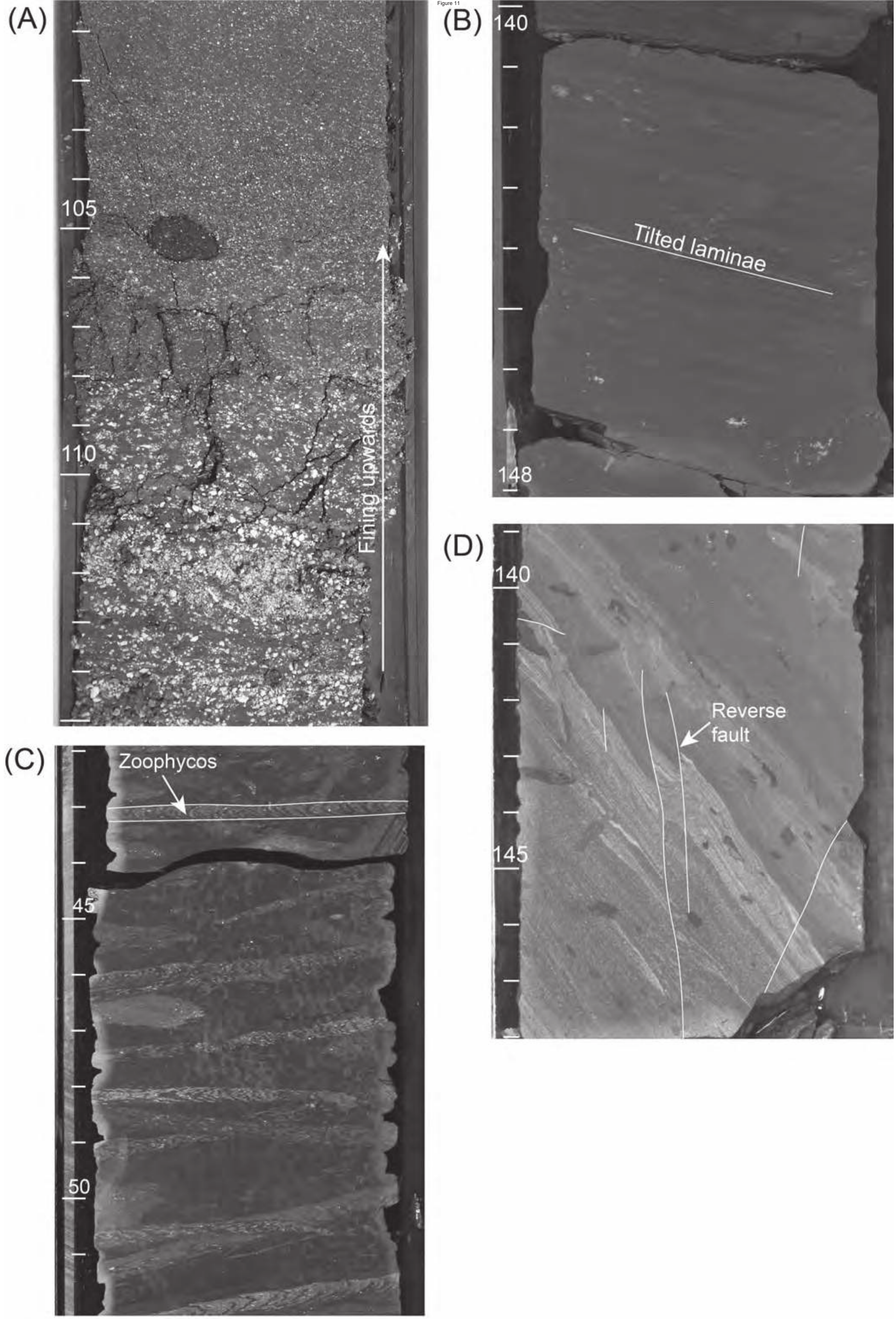

Figure 11
Dailey et al.

Figure 12

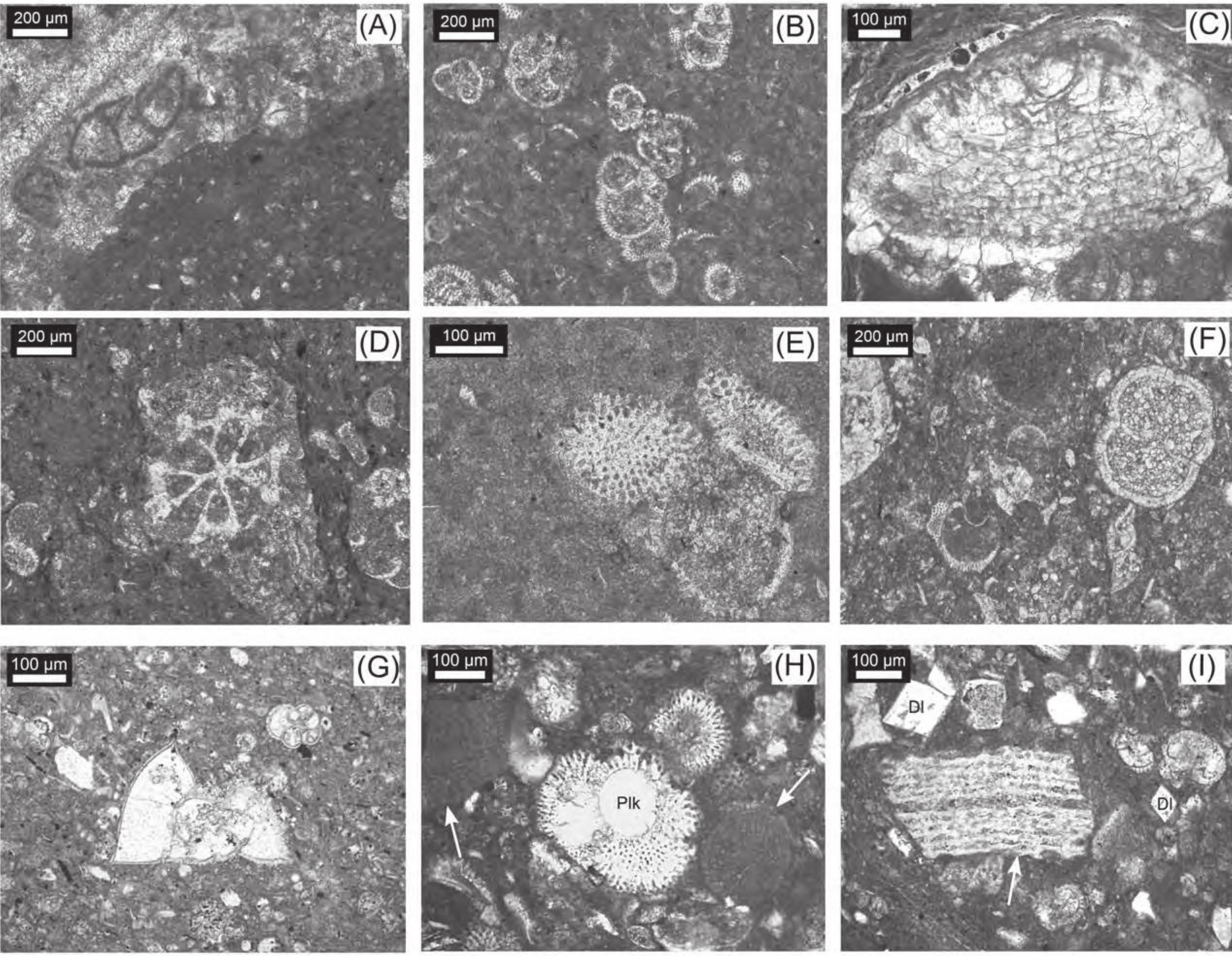

Figure 12
Dailey et al.

Figure 13

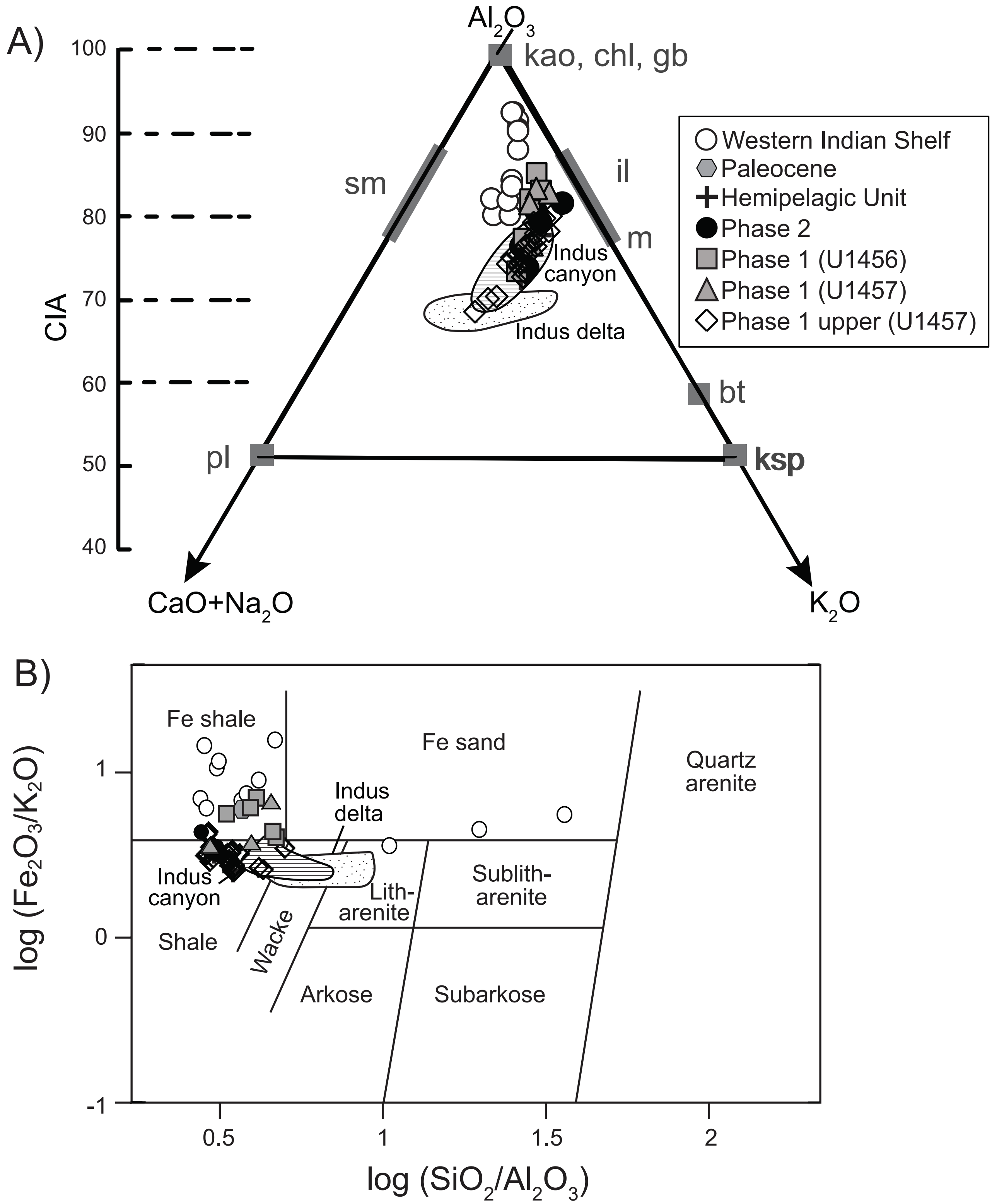

Figure 13
Dailey et al.

Figure 14

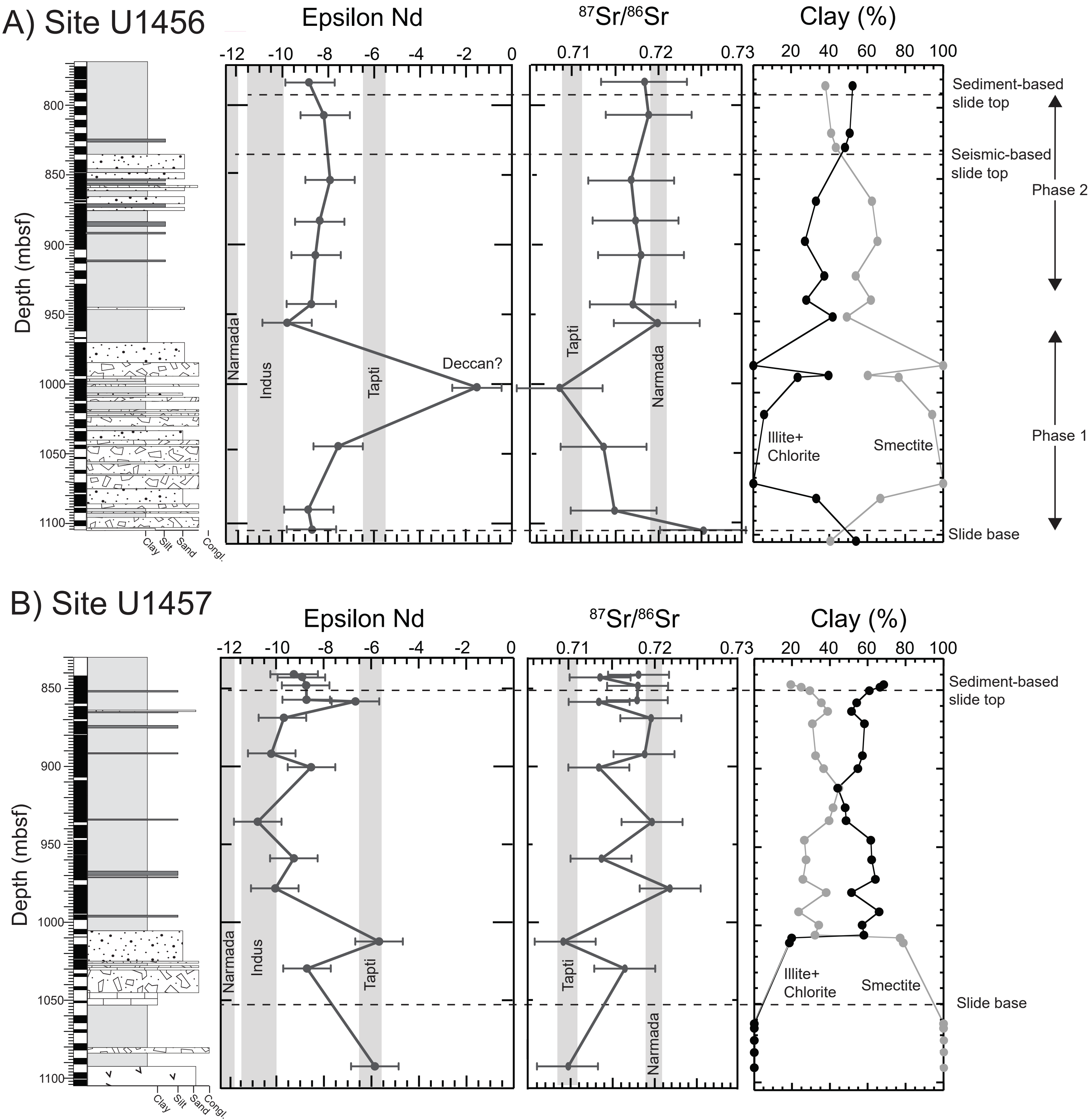

Figure 14
Dailey et al.

Figure 15

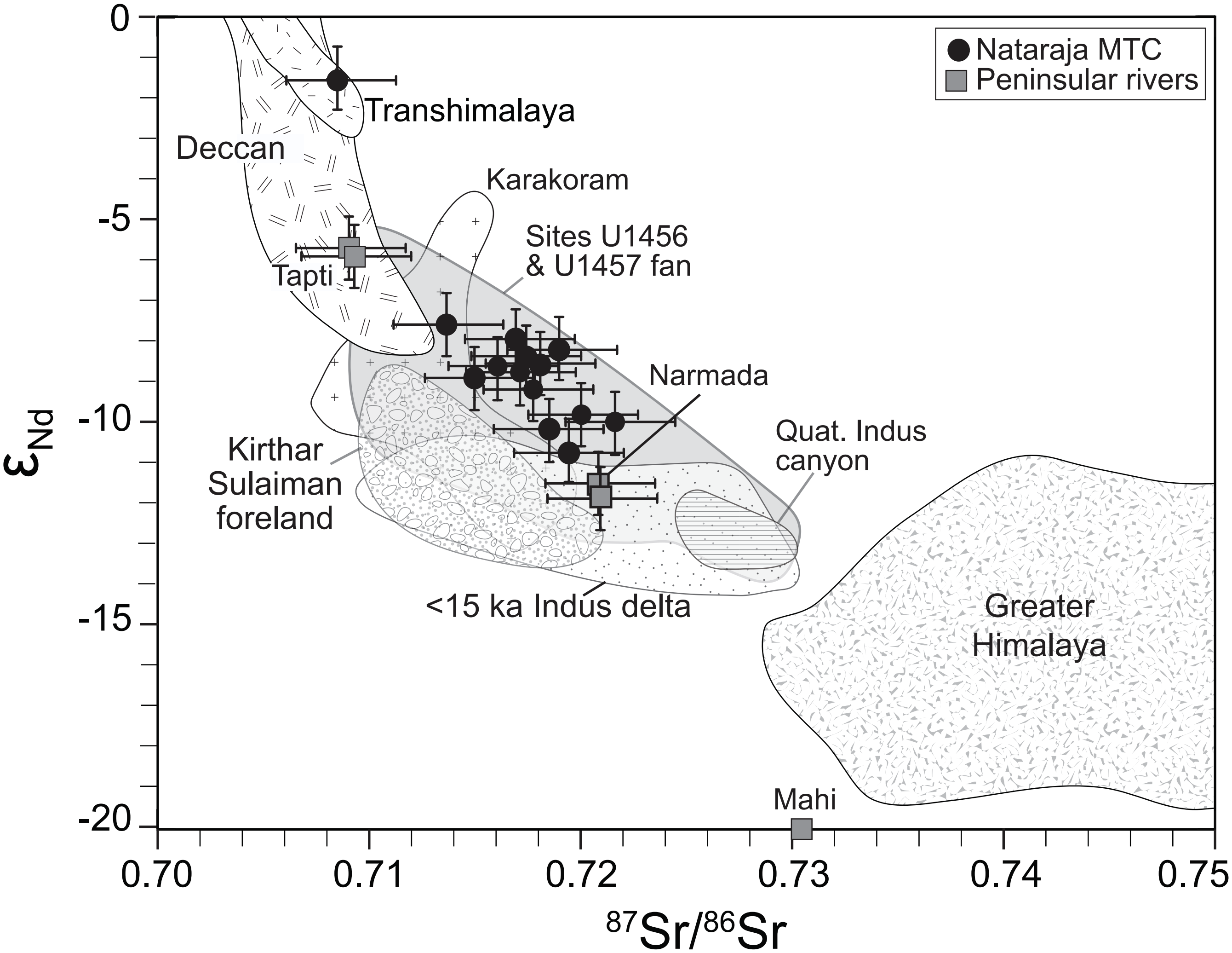

Figure 15
Dailey et al.

Figure 16

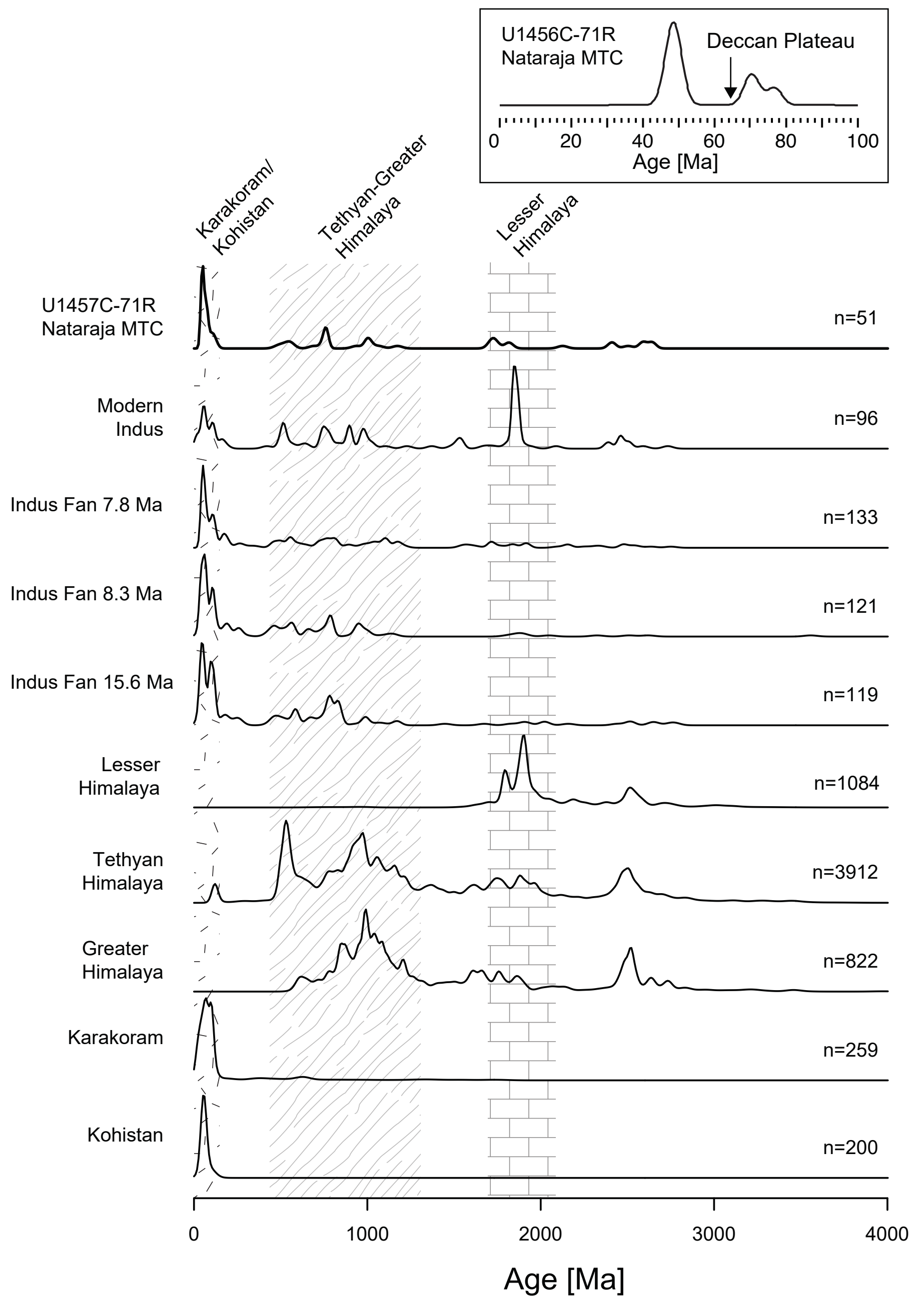

Figure 16
Dailey et al.

Figure 17

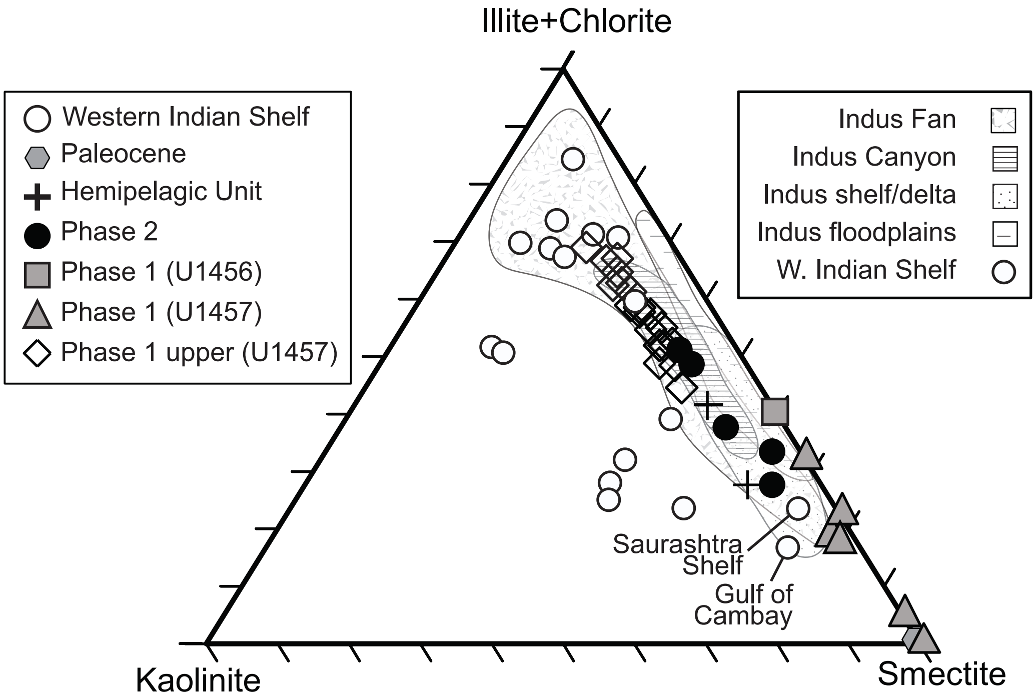

Figure 17
Dailey et al.

Figure 18

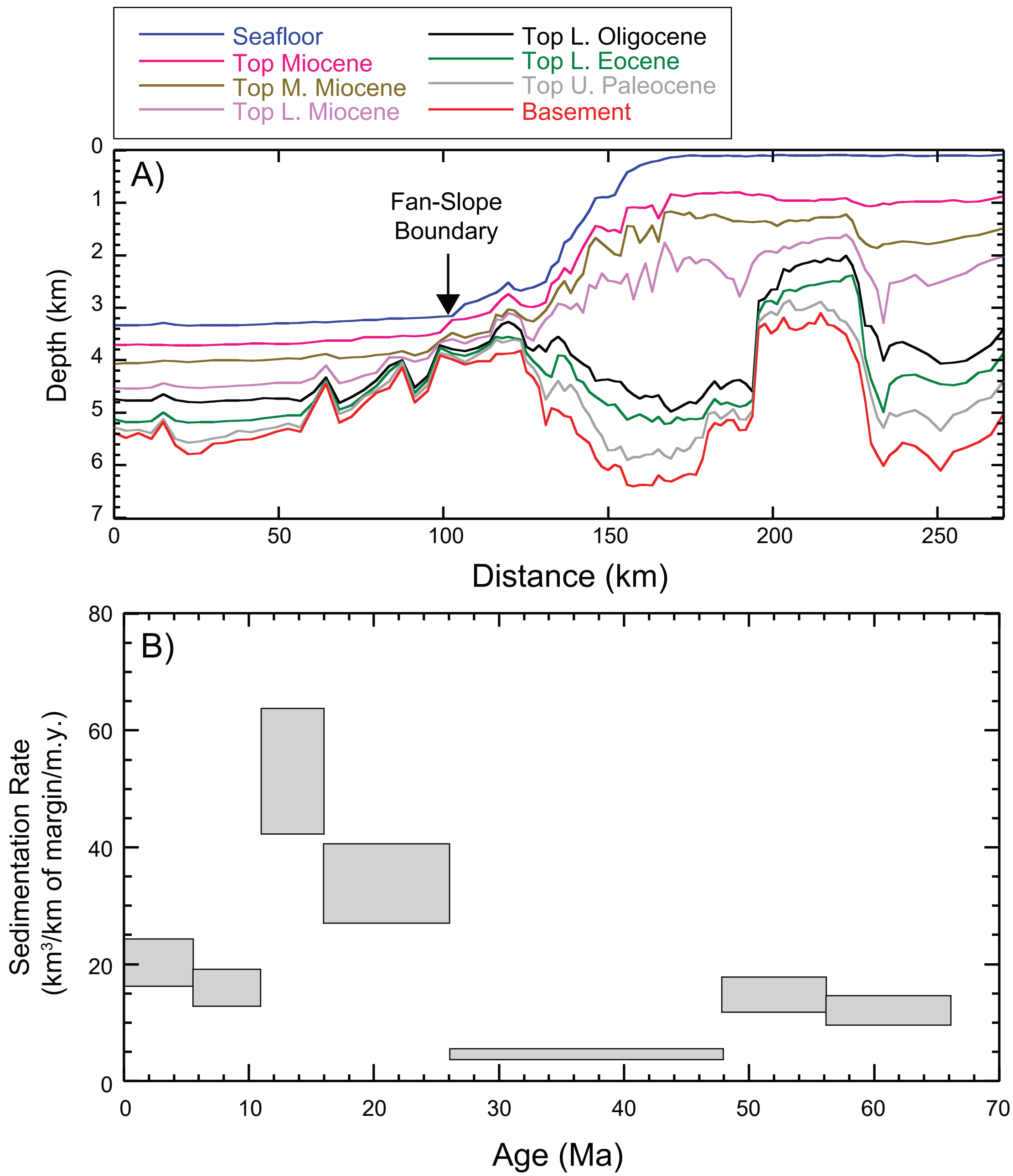

Figure 18
Dailey et al

Figure 19

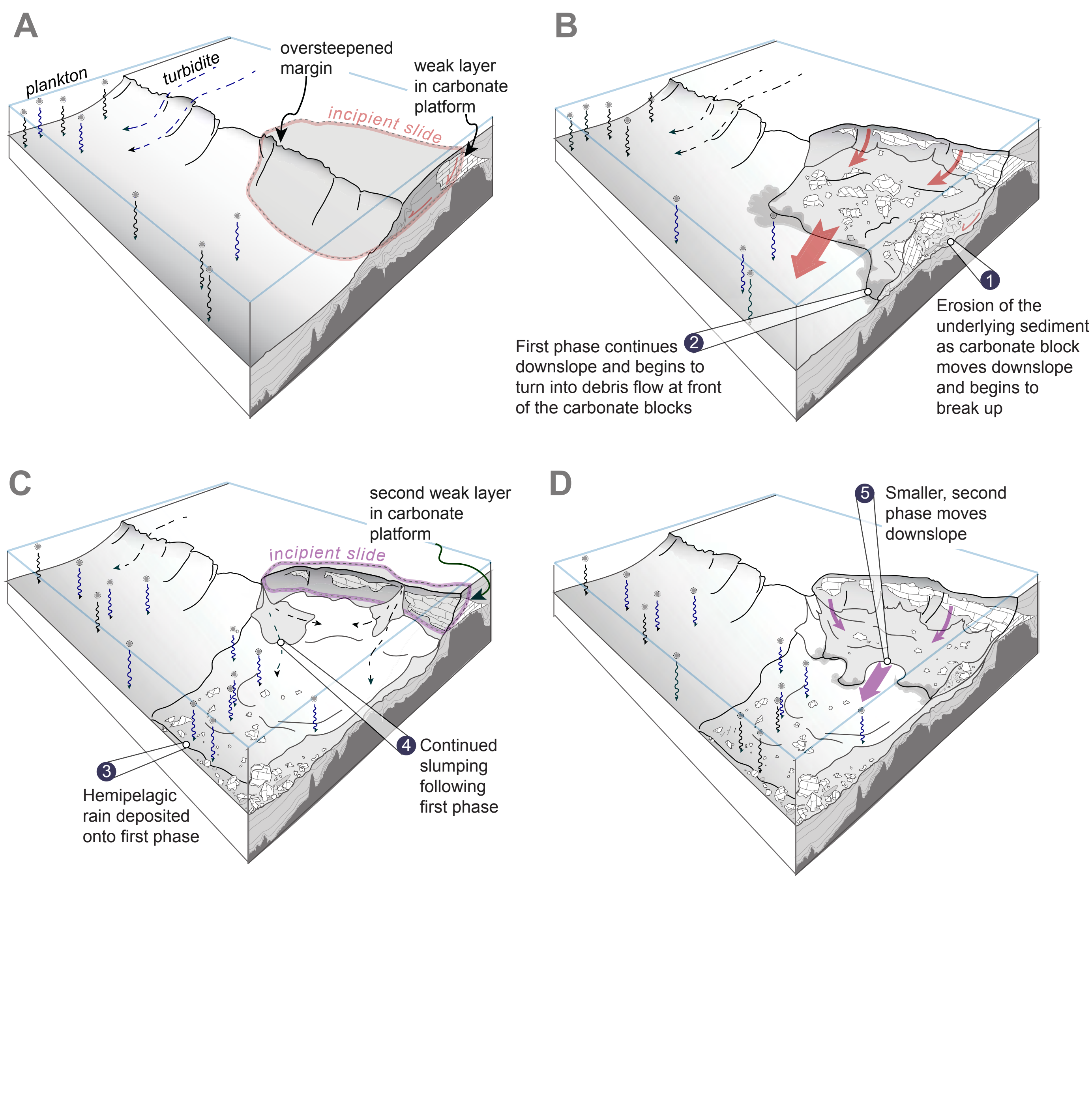

Figure 19
Dailey et al

Sample	Depth (mbsf)	P_2O_5 (%)	SiO2 (%)	MnO (%)	Fe_2O_3 (%)	MgO (%)	Al_2O_3 (%)	TiO_2 (%)	CaO (%)	Na_2O (%)	K_2O (%)	Zr (ppm)	Sr (ppm)	Ba (ppm)
IODP U1456D														
35R-4, 107-122 cm	784.47	0.18	48.71	0.09	8.98	3.75	15.80	0.98	0.32	0.15	2.87	162.01	119.59	403.54
38R-1, 22-24 cm	808.00	0.12	52.99	0.04	7.93	3.33	17.12	1.12	0.19	0.40	2.98	152.43	96.48	431.06
42R-6, 40-42 cm	854.30	0.13	53.39	0.05	8.56	4.15	16.21	0.97	0.18	0.69	3.34	162.15	82.60	368.68
46R-4, 8-10 cm	883.40	0.12	53.59	0.04	8.33	3.17	16.77	1.44	0.27	0.64	2.90	199.20	89.80	404.49
49R-1, 50-52 cm	908.00	0.12	49.57	0.06	9.50	3.01	17.18	1.51	0.54	0.38	2.72	178.69	125.28	414.05
52R-5, 65-67 cm	943.10	0.10	56.31	0.04	6.78	4.13	15.81	1.00	0.20	0.77	3.22	204.61	80.95	350.21
54R-1, 5-7 cm	956.50	0.12	53.22	0.04	8.28	3.18	17.09	1.29	0.23	0.48	3.09	166.90	90.29	366.60
59R-5, 10-12 cm	1002.60	0.09	54.77	0.05	7.50	3.17	11.51	0.71	1.31	0.55	2.30	171.54	738.40	2088.35
60R-1, 109-111 cm	1006.50	0.26	53.12	0.10	6.96	3.37	11.39	0.74	1.48	0.39	1.98	82.44	308.40	1806.13
IODP U1456E														
9R-4, 64-66 cm	1021.00	0.04	51.60	0.07	8.54	3.43	12.40	0.89	1.63	0.15	1.56	159.79	282.36	1890.01
12R-1, 112-114 cm	1044.70	0.07	51.45	0.03	8.85	3.25	12.89	0.89	1.25	0.28	1.84	181.84	108.74	736.09
17R-7, 42-44 cm	1090.10	0.06	49.46	0.05	9.64	3.26	14.60	1.05	1.21	0.20	2.17	159.60	108.94	1250.60
IODP 1457C														
68R-7, 128-130 cm	842.50	0.11	56.57	0.04	7.16	3.42	16.51	1.05	0.20	0.74	2.89	168.76	82.06	409.00
69R- 4, 104-107 cm	846.53	0.15	53.50	0.17	7.60	4.92	15.50	0.91	1.30	0.65	2.84	176.97	100.61	346.80
69R-7, 13-16 cm	850.38	0.12	51.61	0.08	8.59	3.55	16.02	1.02	0.65	0.50	3.09	161.96	104.08	385.13
70R- 1, 6-8 cm	851.70	0.12	54.35	0.04	8.05	3.18	17.25	1.22	0.43	0.56	3.20	154.32	85.26	416.50
70R-5, 95-98 cm	858.16	0.34	53.30	0.29	7.90	4.85	14.87	0.86	1.05	0.67	2.84	169.51	105.17	344.01
71R-1, 7-9 cm	861.50	0.12	52.49	0.04	8.26	3.36	17.39	1.20	0.30	0.37	3.12	143.35	73.07	337.56
71R-2, 109-111 cm	863.49	0.17	50.69	0.11	6.35	3.18	13.48	0.97	7.89	0.66	2.39	191.88	317.03	305.86
72R- 1, 107-110 cm	871.49	0.14	51.68	0.10	8.23	3.53	16.34	1.04	2.21	0.46	2.94	173.34	142.98	346.71
73R-1, 10-12 cm	857.78	0.11	53.52	0.03	8.18	3.28	17.40	1.12	0.09	0.38	3.39	156.13	69.86	357.88
74R-2, 19-21 cm	891.75	0.12	62.72	0.03	5.73	2.76	14.14	0.96	0.50	1.00	2.67	216.07	93.56	370.40
75R-1, 36-40 cm	900.06	0.15	50.12	0.20	8.51	4.00	16.01	0.98	2.34	0.28	2.91	162.80	155.71	325.69
76R- 1, 90-92 cm	911.89	0.15	58.24	0.04	7.05	3.10	16.64	1.01	0.42	0.60	2.98	183.48	83.48	333.03
76R- 3, 44-47 cm	912.57	0.16	49.16	0.11	9.53	3.67	16.17	1.21	1.95	0.43	2.69	176.56	136.57	344.65
77R- 2, 3-5 cm	923.50	0.13	53.97	0.04	8.05	3.30	17.02	1.21	0.28	0.43	2.93	171.88	78.31	359.82
77R- 5, 26-29 cm	924.94	0.11	50.07	0.09	8.35	3.60	16.23	1.00	3.02	0.38	2.88	162.60	188.13	320.07
78R- 4, 25-28 cm	933.28	0.14	49.34	0.13	9.62	3.79	16.33	1.17	1.61	0.39	2.80	178.48	132.21	305.89
78R, 5, 50-52 cm	933.78	0.12	56.60	0.03	6.28	3.10	15.49	1.00	0.30	0.68	2.95	182.32	81.19	325.06
79R-5, 120-122	945.74	0.15	58.44	0.04	7.06	3.16	16.02	1.02	0.40	0.66	3.11	215.88	81.25	298.55
81R-1, 30-32 cm	958.20	0.15	53.22	0.12	7.45	3.46	14.95	0.90	3.36	0.45	2.77	179.71	157.01	270.30
81R-1, 42-44 cm	958.32	0.15	57.32	0.05	7.19	3.34	16.27	0.97	0.42	0.62	3.15	176.67	81.33	279.34
82R-3, 6-9 cm	970.66	0.15	58.78	0.13	6.10	2.96	11.45	0.73	4.59	0.93	2.13	246.76	168.04	245.10
82R-3, 89-91 cm	971.55	0.17	62.47	0.04	6.40	2.99	14.53	0.96	0.62	0.95	2.88	222.25	94.57	306.87
83R-1, 61-63 cm	978.00	0.10	52.09	0.03	7.98	3.13	17.49	1.25	0.16	0.35	3.06	168.56	67.93	282.34
84R-6, 101-103 cm	991.90	0.14	56.77	0.06	7.12	3.88	15.83	0.90	0.28	0.69	3.31	185.01	78.23	266.53
85R- 1, 60-62 cm	998.40	0.12	57.92	0.05	7.09	3.98	16.02	0.92	0.29	0.71	3.36	184.78	82.51	274.00
85R-3, 46-49 cm	999.74	0.16	53.58	0.15	7.86	4.65	15.32	0.89	0.99	0.72	3.21	185.22	116.33	261.00
86R-2, 44-47 cm	1008.04	0.11	18.69	0.07	2.73	1.75	6.14	0.31	31.32	0.07	0.95	57.03	720.11	611.45
87R-1, 14-18 cm	1011.22	0.10	15.76	0.07	2.11	1.45	5.20	0.24	32.94	0.08	0.71	47.83	649.62	1357.92
89R-2, 57-59 cm	1027.62	0.08	52.64	0.06	8.63	3.41	11.45	0.76	1.93	0.26	1.63	94.10	222.78	1315.27
89R-3, 119-121 cm	1029.30	0.05	52.31	0.03	7.46	4.03	13.01	0.77	0.90	0.43	2.41	138.94	82.01	308.97
96R-1, 62-66 cm	1090.74	0.09	47.67	1.10	10.46	3.37	12.29	0.95	0.92	0.49	2.22	139.86	113.58	102.65

Table 2

Sample	$^{87}Sr/^{86}Sr$	$^{143}Nd/^{144}Nd$	Epsilon Nd
IODP U1456D			
35R-4, 107-122 cm	0.718548	0.512186	-8.8
38R-1, 22-24 cm	0.719026	0.512219	-8.2
42R-6, 40-42 cm	0.716960	0.512233	-7.9
46R-4, 8-10 cm	0.717475	0.512210	-8.3
49R-1, 50-52 cm	0.718123	0.512200	-8.5
52R-5, 65-67 cm	0.717166	0.512191	-8.7
54R-1, 5-7 cm	0.720084	0.512137	-9.8
59R-5, 10-12 cm	0.708516	0.512560	-1.5
IODP U1456E			
12R-1, 112-114 cm	0.713705	0.512251	-7.5
17R-7, 42-44 cm	0.715006	0.512184	-8.9
19R-CC, 17-22 cm	0.725510	0.512193	-8.7
IODP 1457C			
68R-7, 128-130 cm	0.717787	0.512169	-9.1
69R-1, 100-104 cm	0.713055	0.512187	-8.8
69R-5, 136-148 cm	0.717709	0.512196	-8.6
70R-4, 137-152 cm	0.717619	0.512197	-8.6
70R-5, 95-97 cm	0.712897	0.512305	-6.5
71R-6, 18-28 cm	0.719332	0.512147	-9.6
74R-2, 19-21 cm	0.718539	0.512119	-10.1
75R-1, 36-40 cm	0.712895	0.512207	-8.4
78R, 5, 50-52 cm	0.719460	0.512089	-10.7
81R-1, 30-32 cm	0.713224	0.512169	-9.1
83R-1, 61-63 cm	0.721653	0.512128	-9.9
87R-1, 14-18 cm	0.708510	0.512357	-5.5
89R-3, 119-121 cm	0.716107	0.512198	-8.6
96R-1, 62-66 cm	0.709144	0.512348	-5.7

Table 3

Sample	Facies	Grain size (μm)	% fine tail	% class analyzed	% coarse tail	n° transparent HM	tot. grains counted	HMC %weight	tHM% weight	zircon	tourmaline	rutile	anatase/brookite	apatite	titanite
Tapti River	Sand bar	15-500	15%	78%	7%	215	309	24	17	0	0	0	0	0	1
1456E-4R-1, 110 cm	Packstone	15-500	63%	37%	0.1%	209	3336	0.08	0.02	5	13	2	1	24	10
1456E-7R-1, 80 cm	Packstone	15-500	46%	54%	0.2%	21	1449	0.06	0.00	5	5	0	0	10	5
1456E-15R-1, 61 cm	Breccia	15-500	52%	33%	15%	68	2557	0.04	0.00	10	4	1	0	16	13
1456E-17R-4, 131 cm	Breccia	15-500	50%	24%	26%	64	1144	0.05	0.01	6	6	3	0	22	8
1457C-88R-4, 58 cm	Packstone	15-500	42%	53%	5%	216	819	0.14	0.08	4	6	1	1	11	9

Sample	andalusite	kyanite	sillimanite	amphibole	green augite	Cr-spinel	Total	ZTR	% transparent	% opaque	% Fe oxide	% Ti oxide	% HM turbid	% rock fragments	% soils & turbid
Tapti River	0	0	1	2	92	0.0	4.7	0	70	24	4	0	0	1	0
1456E-4R-1, 110 cm	0.5	2	0	2	1	4	90.4	20	6	8	7	1	0	0	0
1456E-7R-1, 80 cm	0	0	0	10	48	0	42.9	10	1	61	0	0	0	0	0
1456E-15R-1, 61 cm	3	1	0	0	6	3	86.8	16	3	19	5	0	0	0	0
1456E-17R-4, 131 cm	0	0	0	3	6	2	89.1	16	6	10	7	0	0	0	0
1457C-88R-4, 58 cm	0.5	1	0	8	1	2	87.5	11	26	11	5	1	0	0	0

Table 3

barite	diaspore	epidote	garnet	chloritoid	staurolite	% phosphate	% chlorite	% biotite	% carbonates	% light minerals	Total
0	0	2	1	0	0	0	0	0	0	1	100
3	0	9	15	8	1	35	6	6	30	1	100
5	0	0	14	0	0	17	0	1	19	0	100
4	0	9	21	3	4	57	1	1	13	1	100
5	0	9	25	3	2	59	1	3	10	3	100
3	0.5	30	18	4	0.5	19	6	12	15	5	100

Table 4

Preferred Age (Ma)	2 -sigma	2 +sigma	Concordant Scans	^{207}Pb/^{235}U	2 sigma	^{206}Pb/^{238}U	2 sigma	^{207}Pb/^{206}Pb	2 sigma	Concordant Scans: Ages ^{206}Pb/^{238}U Age (Ma)	2 -sigma	2 +sigma	^{207}Pb/^{206}Pb Age (Ma)	2 -sigma	2 +sigma
47.01	1.37	1.37	64	0.05045	0.00660	0.00732	0.00021	0.04999	0.00657	47.01	1.37	1.37	194.64	320.86	292.11
47.33	1.26	1.26	64	0.05143	0.00657	0.00737	0.00020	0.05062	0.00651	47.33	1.26	1.26	223.55	311.81	284.54
47.79	1.85	1.85	46	0.04993	0.00845	0.00744	0.00029	0.04866	0.00834	47.79	1.85	1.85	131.60	263.20	379.94
48.02	1.73	1.73	46	0.05000	0.00839	0.00748	0.00027	0.04850	0.00826	48.02	1.73	1.73	123.77	247.55	378.11
48.53	1.99	1.99	47	0.05389	0.00852	0.00756	0.00031	0.05172	0.00821	48.53	1.99	1.99	273.19	385.93	344.89
48.99	3.14	3.14	20	0.05734	0.01738	0.00763	0.00049	0.05452	0.01668	48.99	3.14	3.14	392.40	771.22	621.88
49.14	1.90	1.90	47	0.05466	0.00857	0.00765	0.00030	0.05181	0.00818	49.14	1.90	1.90	277.18	383.24	342.72
49.17	1.87	1.87	48	0.05409	0.00847	0.00766	0.00029	0.05124	0.00809	49.17	1.87	1.87	251.45	384.95	344.15
49.35	3.20	3.20	19	0.05756	0.01799	0.00769	0.00050	0.05432	0.01715	49.35	3.20	3.20	384.50	769.00	640.63
50.14	2.00	2.00	37	0.05946	0.01166	0.00781	0.00031	0.05524	0.01089	50.14	2.00	2.00	421.88	472.90	412.18
50.28	1.94	1.94	34	0.05859	0.01191	0.00783	0.00030	0.05427	0.01111	50.28	1.94	1.94	382.12	496.18	429.90
70.08	2.50	2.50	38	0.07447	0.01329	0.01093	0.00039	0.04941	0.00889	70.08	2.50	2.50	167.37	334.74	395.24
70.15	2.28	2.28	39	0.07461	0.01292	0.01094	0.00036	0.04946	0.00865	70.15	2.28	2.28	169.51	339.03	384.58
70.16	2.26	2.26	43	0.07510	0.01242	0.01094	0.00035	0.04977	0.00830	70.16	2.26	2.26	184.37	368.75	366.98
72.23	2.74	2.74	37	0.08171	0.01524	0.01127	0.00043	0.05259	0.00993	72.23	2.74	2.74	311.22	460.83	403.35
76.83	3.05	3.05	68	0.08023	0.00532	0.01199	0.00048	0.04853	0.00298	76.83	3.05	3.05	125.30	148.01	141.61
77.15	3.05	3.05	67	0.08014	0.00533	0.01204	0.00048	0.04828	0.00299	77.15	3.05	3.05	112.82	149.29	142.79
100.16	3.15	3.15	59	0.10617	0.00460	0.01566	0.00050	0.04917	0.00188	100.16	3.15	3.15	156.18	90.86	88.40
100.99	2.82	2.82	62	0.10697	0.00434	0.01579	0.00044	0.04914	0.00181	100.99	2.82	2.82	154.32	87.35	85.07
118.08	5.47	5.47	58	0.12988	0.01607	0.01849	0.00086	0.05096	0.00637	118.08	5.47	5.47	238.93	301.60	276.00
120.22	5.26	5.25	58	0.13169	0.01594	0.01882	0.00083	0.05074	0.00622	120.22	5.26	5.25	228.91	296.48	271.72
484.75	13.50	13.48	120	0.60703	0.01998	0.07810	0.00226	0.05637	0.00139	484.75	13.50	13.48	467.11	55.05	54.12
519.35	18.13	18.10	111	0.67939	0.02913	0.08390	0.00305	0.05873	0.00208	519.35	18.13	18.10	557.10	78.23	76.36
547.29	23.73	23.68	71	0.73343	0.05847	0.08861	0.00400	0.06003	0.00498	547.29	23.73	23.68	604.79	184.88	174.70
565.78	24.78	24.73	72	0.75974	0.06307	0.09173	0.00419	0.06007	0.00510	565.78	24.78	24.73	606.01	189.07	178.44
691.81	24.28	24.23	17	1.05756	0.04642	0.11329	0.00419	0.06771	0.00244	691.81	24.28	24.23	859.54	75.81	74.02
742.77	112.79	111.81	5	1.28928	0.25300	0.12212	0.01955	0.07657	0.01460	742.77	112.79	111.81	1109.98	406.32	358.96
754.15	21.48	21.45	92	1.08175	0.06391	0.12410	0.00374	0.06322	0.00367	754.15	21.48	21.45	715.56	125.85	121.02
762.15	21.70	21.67	99	1.13684	0.04166	0.12550	0.00379	0.06570	0.00233	762.15	21.70	21.67	796.76	75.25	73.49
764.53	19.53	19.50	84	1.09582	0.06500	0.12592	0.00341	0.06312	0.00375	764.53	19.53	19.50	712.23	128.77	123.72
766.14	25.46	25.41	41	1.19877	0.06376	0.12620	0.00444	0.06889	0.00368	766.14	25.46	25.41	895.57	112.18	108.28
937.35	22.90	22.86	98	1.55283	0.04656	0.15651	0.00410	0.07196	0.00189	937.35	22.90	22.86	984.77	53.80	52.88
997.31	29.09	29.03	97	1.73089	0.05731	0.16732	0.00526	0.07503	0.00227	997.31	29.09	29.03	1069.26	61.51	60.31
1002.01	40.31	40.18	126	1.68389	0.07518	0.16817	0.00729	0.07262	0.00249	1002.01	40.31	40.18	1003.43	70.40	68.84
1017.09	21.65	21.62	104	1.79155	0.04889	0.17090	0.00393	0.07603	0.00212	1017.09	21.65	21.62	1095.83	56.39	55.38
1064.57	23.22	23.18	79	1.90134	0.06993	0.17956	0.00424	0.07680	0.00272	1064.57	23.22	23.18	1115.94	71.52	69.90
1173.37	25.27	25.22	68	2.30640	0.06114	0.19964	0.00470	0.08379	0.00200	1173.37	25.27	25.22	1287.68	46.92	46.21
1703.26	43.19	42.57	107	4.30372	0.10657	0.29906	0.00565	0.10437	0.00243	1686.66	28.06	28.00	1703.26	43.19	42.57
1719.35	37.26	36.80	121	4.36640	0.09580	0.30078	0.00576	0.10529	0.00212	1695.16	28.56	28.50	1719.35	37.26	36.80
1734.05	45.62	44.93	35	4.14546	0.12716	0.28328	0.00809	0.10613	0.00262	1607.86	40.70	40.57	1734.05	45.62	44.93
1751.80	44.50	43.84	92	4.44995	0.11308	0.30116	0.00596	0.10717	0.00259	1697.04	29.55	29.48	1751.80	44.50	43.84
1809.44	50.74	49.89	114	4.95575	0.14377	0.32495	0.00818	0.11061	0.00306	1813.86	39.84	39.72	1809.44	50.74	49.89
1824.80	35.56	35.14	85	4.65207	0.13339	0.30247	0.00829	0.11155	0.00217	1703.54	41.07	40.94	1824.80	35.56	35.14
2126.41	196.81	184.41	11	6.01281	0.90134	0.33006	0.05028	0.13213	0.01436	1838.66	246.02	241.41	2126.41	196.81	184.41
2404.03	46.88	46.13	115	9.69673	0.27654	0.45314	0.01182	0.15520	0.00425	2409.19	52.52	52.31	2404.03	46.88	46.13
2417.39	46.37	45.64	103	9.10358	0.25984	0.42209	0.01083	0.15643	0.00424	2269.95	49.21	49.02	2417.39	46.37	45.64
2504.10	52.23	51.30	45	9.98345	0.42634	0.43973	0.01793	0.16466	0.00507	2349.43	80.51	80.01	2504.10	52.23	51.30
2584.49	44.66	43.98	101	11.36799	0.39304	0.47726	0.01606	0.17275	0.00459	2515.34	70.28	69.90	2584.49	44.66	43.98
2594.62	47.11	46.35	96	11.43402	0.43489	0.47713	0.01803	0.17380	0.00487	2514.75	78.95	78.47	2594.62	47.11	46.35
2636.60	60.15	58.92	103	11.99958	0.44152	0.48826	0.01801	0.17824	0.00639	2563.14	78.26	77.79	2636.60	60.15	58.92
2649.00	61.39	60.11	102	12.03610	0.46870	0.48610	0.01915	0.17958	0.00657	2553.78	83.33	82.80	2649.00	61.39	60.11

Table 5

Sample	Smectite (%)	Chlorite (%)	Illite (%)	Kaolinite (%)	Palygorskite (%)
IODP U1456D					
35R-4, 107-122 cm	37.6	18.7	33.0	9.6	0.0
39R-1, 12-14 cm	40.9	13.8	36.8	8.2	0.0
40R-1, 60-62 cm	43.1	13.9	8.0	8.1	34.1
43R-7, 2-4 cm	62.2	12.9	19.9	4.4	0.0
47R-4, 58-60 cm	65.2	13.8	13.4	7.3	0.0
50R-1, 31-33 cm	53.8	15.5	21.9	8.5	0.0
51R-6, 20-22 cm	61.4	11.9	15.8	10.0	0.0
53R-1, 5-7 cm	49.1	14.6	27.0	8.7	0.0
57R-7, 75-77 cm	53.1	8.4	26.5	0.0	10.6
58R-2, 2-4 cm	69.9	3.8	17.5	0.0	6.7
61R-1, 40-42 cm	91.9	0.8	4.8	0.0	2.5
IODP U1456E					
5R-2, 25-27 cm	100.0	0.0	0.0	0.0	0.0
14R-1, 75-77 cm	96.9	0.0	0.0	0.0	0.0
16R-2, 5-7 cm	54.8	4.6	22.5	0.0	18.0
19R-CC, 17-22 cm	40.0	25.0	28.3	5.1	0.0
IODP U1457C					
69R-4, 104-106 cm	17.2	27.2	33.5	10.9	9.9
69R-6, 13-15 cm	23.2	26.7	35.6	8.2	4.8
69R-7, 112-114 cm	29.0	22.6	37.4	9.7	0.0
70R-5, 95-97 cm	32.3	18.8	30.6	9.6	7.6
71R-2, 109-111 cm	38.5	17.9	33.2	9.7	0.0
72R-1, 107-109 cm	30.3	23.2	34.2	10.8	0.0
74R-2, 25-27 cm	31.8	23.1	33.2	10.3	0.0
75R-1, 36-40 cm	36.2	21.0	33.0	8.4	0.0
76R-3, 44-46 cm	44.3	17.9	25.8	11.2	0.0
77R-5, 26-28 cm	41.3	19.2	28.5	10.1	0.0
78R-4, 25-27 cm	39.1	19.9	28.1	11.9	0.0
79R-5, 129-131 cm	26.2	23.1	37.9	11.7	0.0
81R-1, 30-32 cm	27.1	22.2	39.3	10.4	0.0
82R-3, 6-8 cm	25.5	20.9	42.6	10.2	0.0
83R-2, 18-20 cm	37.7	16.8	34.1	10.4	0.0
84R-3, 143-145 cm	23.1	25.0	39.9	10.4	0.0
85R-3, 46-48 cm	31.1	15.8	36.2	8.1	8.1
86R-1,6-8 cm	29.6	18.2	35.3	9.1	6.9
86R-2, 44-46 cm	75.5	5.1	14.4	3.1	1.5
87R-1, 14-18 cm	77.0	4.5	13.6	2.6	1.5
93R-1, 50-52 cm	100.0	0.0	0.0	0.0	0.0
93R-3, 50-52 cm	100.0	0.0	0.0	0.0	0.0
94R-2, 55-57 cm	100.0	0.0	0.0	0.0	0.0
95R-1, 12-14 cm	100.0	0.0	0.0	0.0	0.0

96R-1, 62-66 cm	100.0	0.0	0.0	0.0	0.0

Table 6

Stratigraphic interval	Age at base of interval	Interval velocity (km/s)
H7	Top Miocene	1.70
H6	Top M. Miocene	2.20
H5	Top L. Miocene	2.40
H4	Top. L. Oligocene	2.45
H3	Top. L. Eocene	2.50
H2	Top U. Paleocene	2.60
H1	Basement (66 Ma)	2.65